J Mater Sci (2009) 44:3319–3343
DOI 10.1007/s10853-009-3394-y

REVIEW

On the shock compression of polycrystalline metals

N. K. Bourne · J. C. F. Millett · G. T. Gray III

Received: 20 November 2008 / Accepted: 11 March 2009 / Published online: 24 April 2009

Abstract At the present time, materials are being considered for use in increasingly extreme environments; extreme in terms of both the magnitude of the imposed pressures and stresses they encounter and the speed of the loading applied. Recent advances in understanding the continuum behaviour of condensed matter have been made using novel loading and ultrafast diagnostics. This insight has indicated that in the condensed phase, the response is driven by the defect population existing within the microstructure which drives plastic flow in compression as well as damage evolution and failure processes. This article discusses shock compression results, focusing upon research conducted on cubic-structured metals but also giving an overview of results on hexagonal-close-packed (HCP) metals and alloys. In the past, shock physics has treated materials as homogeneous continua and has represented the compressive behaviour of solids using an adaptation of solid mechanics. It is clear that the next generation of constitutive models must treat physical mechanisms operating at the micro- and mesoscale to adequately describe metals for applications under extreme environments. Derivation of such models requires idealized modes of loading which limits the range of hydrostatic or impact driven experimental techniques available to four principle groups. These are laser-induced plasma loading, Z pinch devices, compressed gas and powder-driven launchers and energetic drives and diamond anvil cells (DACs). Whilst each technique or device discussed brings unique advantages and core competencies, it will be shown that launchers are most capable of covering the spectrum of important and relevant mechanisms since only they can simultaneously access the material microstructural 'bulk' dimensions and timescales that control behaviour observed at the continuum. Shock experiments on a selection of metals whose response is regarded as typical are reviewed in this article, and sensors and techniques are described that allow the interpretation of the compression that results from idealized step loading on a target. Real-time imaging or X-ray techniques cannot at present access bulk states at the correct microstructural resolution, over a macroscopic volume or at rates that would reveal mechanisms occurring. It is controlled recovery experiments that provide the link between the microstructure and the continuum state that facilitates understanding of the effect of mesoscale properties upon state variables. Five metals are tracked through various shock-loading techniques which show the following characteristic deformation features; a low Peierls stress and easy slip allow FCC materials to develop dislocation cells and work-harden during the shock process, whereas the higher resistance to dislocation motion in BCC-structured materials and the lower symmetry in HCP metals slows the development of the microstructure and favours deformation twinning as an additional deformation mechanism to accommodate shock compression. Thus not only energy thresholds, but also operating kinetics, must be understood to classify the response of metals and alloys to extreme loading environments. Typical engineering materials possess a baseline microstructure but also a population of defects within their volumes. It is the understanding of these statistical physical relationships and their effects upon deformation mechanisms and defect storage processes that will drive the development of materials for use under extreme conditions in the future.

N. K. Bourne (✉) · J. C. F. Millett
AWE, Aldermaston, Reading RG7 4PR, UK
e-mail: neil.bourne@mac.com

G. T. Gray III
MST-8, Los Alamos National Laboratory, Los Alamos, NM 87545, USA

Introduction

Understanding materials' response to extreme conditions is an important research goal in the present age. Man is striving to produce greater energy generation capacity in ever-harsher environments and to understand the effect of dynamic loads on existing materials, components and systems and to design new ones for the future using materials with potentially novel microstructures. The shock impulse provides a pump to drive materials' deformation that also allows a window into the mechanisms that lead to plasticity and damage within metals. This review aims to highlight some of the insights into material behaviour that can be extracted through novel loading and ultrafast diagnostics. It assumes the reader is not familiar with the details of the impact physics field so aims to supply key information without resort to mathematical rigour.

Any load driven into a material by whatever means is relieved at some point when the driving stimulus is removed. These released interactions, or the reflection of a compression pulse to generate release of the pressure and thereafter loading in tension, are a subject of interest in their own right and though of importance are not considered in any depth in this review. Suffice to say that their mechanisms and features are a review in themselves sharing many of the features of the loading discussed below in relation to compression. The defect population existing in the microstructure drives both dislocation activation and plastic flow in compression, as well as failure by nucleation and growth of damage [1].

The response of materials to high loading rates has traditionally been of principle interest to the military in an effort to understand ballistic response (to penetrators, shape charges, etc.) from armour systems. More recently, other industries have realized that they require the same knowledge to understand a number of applications of materials and systems. These are dubbed crashworthiness (in the automotive industry) and include bird strike, foreign object damage and blade containment in the aerospace community as well as satellite protection for communications. However, by their very nature, real impact events are complex, both spatially and temporally, since they consist of a projectile of random material, impact velocity and incident angle striking a complex geometrical form, be it an aerofoil, turbine blade or glacis plate in an armour system. As a consequence, it is nearly impossible to gain meaningful materials' data by simply reproducing aspects of such impact events, and hence it is necessary to load materials in simpler geometries where data can be extracted and the loading mode (at least at the continuum) can be quantified. Similar comments apply to impulsive loading onto structures from explosive blast or from a plasma created by a laser loading the surface of a material. Understanding the interaction with the metal in the target is the key to explaining, then understanding and modelling the operative physics and thereafter protecting against its effect.

There is certainly a current need to solve design problems experienced when structures experience dynamic and impact loading. To do this, requires valid, physically based, analytical laws that describe the salient aspects of the dynamic deformation behaviour of materials. At present, numerical codes are approaching such a level of accuracy and proficiency that multiple simulations may be used to examine and iterate design requirements efficiently and in a cost effective manner compared with large-scale laboratory and thereafter system or platform testing programs. However, populating material descriptions found in such codes with suitable analytical models, generally requires knowledge of operating physical mechanisms at the mesoscale. This review will attempt to provide an overview of the present state-of-the-art concerning the shock response of metals focusing upon work done on cubic materials but also providing some results on HCP metals as well. It is hoped that the reader will get a flavour of the physics involved, the experimental techniques utilized, the concerns and the behaviours encountered when a shock propagates through a target and realize the importance of the individual response of materials to such threats particularly when they are placed in a regime where their performance might be an issue.

Researchers across the last two centuries have assembled evidence over many decades of strain rate showing that metals strengthened as loading rate was increased [2–4]. Other treatises have reviewed the development of mechanical testing at intermediate rates over that period so that only a brief summary will be presented here [5–7]. The first publications on investigations of material strength began in 1864 with the work of Tresca [8], who experimentally measured yield criteria for several metals. This was followed in 1870 with the first mathematical description of plasticity by Levy and Saint-Venant [9]. Early studies mapped the behaviour of a series of metals and their alloys and showed that their static properties were different to those obtained under impact conditions. By the end of the nineteenth century it was proven that metals showed higher flow stresses and increased strengths as loading rate increased but it was not until the early part of the twentieth century, that explanation for the observations was being formulated using the concepts of dislocation generation and motion [2, 4]. It was realized that the macroscopic strain rate could be related to the speed of the travelling dislocations (Orowan [10]) and by the onset of the second world war, these concepts were used to determine the yield stress of metals to allow screening for their potential use as armours. Simple impact testing such as that adopted in the

Taylor test, gave a means of quickly ranking materials under relevant conditions and a simple analysis allowed determination of an average dynamic yield strength by this means [11, 12]. Even today, this simple test is used, although now it is to screen the validity and accuracy of materials' models for impact work.

A key advance after the second world war was the development by Kolsky [13] of the original *split* Hopkinson pressure bar. Further adaptation over the following years has used analogous methodology to study materials loaded in tension and torsion. The Hopkinson bar has assumed a key role as the intermediate strain rate experimental testing technique of choice and a series of review articles have very fully described its means of use [14]. To the basic suite of solid materials tests has been added adaptations to the specimen form to allow it to be used to measure the fracture toughness and shear properties of various metals (e.g. [15, 16]).

The key application of present experimental testing efforts is focused on providing the material strength datasets as a function of applied testing variables to which parameters may be derived for the constitutive models of choice to support simulations in modern continuum computer codes. Strain-rate and temperature effects were first included in the empirically based Johnson-Cook and Steinberg-Guinan models [17]. The Hoge–Mukherjee model (HM) [18] incorporated the dislocation dynamics including the Peierls mechanism and also phonon drag at high stress levels. Later advances added more physics directly connected to microstructure, with the Zerilli–Armstrong (ZA) model [19–21] explicitly including the differing strain-rate hardening effects seen in the loading of FCC and BCC metals. The Mechanical threshold stress model (MTS) emphasizes the connection of structure evolution to changes in dislocation density [22–25] whilst the newest of the descriptions, the Preston–Tonks–Wallace model (PTW) [26], uses scale invariance to define the form of the equation set.

These models must show success in the range of micromechanics problems that the solid mechanics and materials modelling communities aim to address. These problems include the ductile–brittle transition [27], fracture toughness properties [15], adiabatic shear banding [28], material responses to ballistic impacts and shock or isentropic compression experiments [29]. Further problems include the debate concerning the transition from slip dominated plasticity to deformation including contributions from twinning which has included much recent work that has not had any clear explanation at present [30–33]. Finally, after an initial compressive stress excursion has ended, further mechanisms follow conditioning the microstructure for later reloading. Amongst such mechanisms are dynamic recrystallization [34, 35] and spallation or fragmentation [36–38].

At quasi-static strain rates ($<10^1$ s^{-1}), samples can be loaded in uniaxial stress, either in compression or tension using servo-hydraulic test machines or under conditions of plane strain for fracture toughness measurements. As strain rate increases (up to ca. 10^4 s^{-1}), uniaxial stress conditions can be maintained in the final stages of the loading, using devices such as the split-Hopkinson pressure bar (SHPB), although now the effects of inertia must be accounted for since releases from the free surfaces must propagate in the initial stages of the loading to ensure stress-state equilibrium. At the highest impact speeds, the state is in one of uniaxial strain where the material is compressed down a single direction and there is no time for further correction to allow for a triaxial state. It is this loading stress state that is important for the type of problem considered here since dynamic loading may only progress on a timescale commensurate with that taken for waves to reach areas of interest from boundaries. Thus initially at the continuum scale, planar loading remains so until waves arrive from the periphery to load the material triaxially. In the initial compression, components of flow and strain are in direction of the incoming impactor. In release and potentially subsequent tension, they are controlled by the geometry of the surfaces surrounding.

Such conditions can be generated either through the use of explosives where the pulse applied is that from a confined high pressure gas, or from interaction of a surface with a laser, where some of the surface is removed and the pulse applied is that from a confined high pressure plasma. However, more commonly it is via the impact of a flat projectile of known response onto a flat, instrumented target such that information can be extracted. Both projectile and target have to be flat and parallel to high precision (ca. ±5 μm over ca. 100 mm in the case of plate impact) and the impact itself must be aligned to the same tolerances. Under these conditions, stress (σ_x) is transmitted as a shock front, behind which conditions of uniaxial strain apply, i.e. all strains (ε) are imposed along the impact axis (x). As a consequence, an axisymmetric stress state also exists to maintain inertial confinement, thus,

$$\varepsilon_x \neq \varepsilon_y = \varepsilon_z = 0, \text{ and, } \sigma_x \neq \sigma_y = \sigma_z \neq 0 \quad (1)$$

where the subscripts y and z are the axes orthogonal to x.

In the elastic range one may express the strain down all the directions using Hooke's law. Substituting in conditions from Eq. 1 yields

$$\sigma_y = \sigma_z = \left[\frac{\nu}{1-\nu}\right]\sigma_x. \quad (2)$$

which relates the three orthogonal stress components in a uniaxially strained material. Typical values for Poisson's ratio, ν, are generally close to one-third for metals so that the lateral stress is about half the longitudinal stress. The

shear stress (τ) of an isotropic material is determined through the relation

$$2\tau = \sigma_x - \sigma_y = \left[\frac{1-2\nu}{1-\nu}\right]\sigma_x, \tag{3}$$

where ν is Poisson's ratio. For such a material the elastic limit in one-dimensional strain is related to the yield stress (Y) through the (3) and for the ideal metal ($\nu = \frac{1}{3}$) the value of the longitudinal stress at yield, the Hugoniot Elastic Limit (HEL) is twice the yield stress measured from a simple tensile test for example. Beyond the HEL the material is in a plastic state and the longitudinal component of the stress, σ_x, rises to a higher value again composed of a deviatoric component, τ, and a hydrostatic confining pressure, p, thus

$$\sigma_x = p + \frac{4}{3}\tau. \tag{4}$$

Any loading at the impact face imposes an instantaneous stress jump that travels at an elastic wave-speed if that amplitude lies below the yield stress. If the imposed stress lies above this value, a plastic front travels forward at a slower speed. Thus a step impulse that results from impact upon a target face decomposes into a wave with two steps travelling at slower and faster speeds, above and below the yield point. Eventually the impact stress becomes so high that the material is plastically compressed to the point where a pulse travels through it faster than the initial elastic pulse did but the work discussed below will be for states where loading is limited to ca. ten times the elastic limit of the material by which point the shock is not overdriven in this manner in the materials considered. A complete description of the physics and thermodynamics of shock deformation is beyond the scope of this article; however, the interested reader is directed to the seminal review article of Davison and Graham [39].

A complete understanding of metal response to an arbitrary loading condition is further complicated by the fact that the majority of engineering alloys are complex multi-phase systems at the mesoscale, where a variety of effects, such as number and type of phases, morphology, distribution and grain size all influence the material response. The philosophy followed here is to start with simpler systems such as pure metals and to describe known effects when microstructure is more controlled at a smaller length scale. Such research has been carried out at low strain rates for many years. However, at intermediate and particularly under the shock-loading regime, the available literature is much less abundant. Further, the traditional shock physics approach treats materials as homogeneous (i.e. structureless) continua. This has provided a qualitatively reasonable means of representing the compressive behaviour of solid materials, which has been adapted into solid mechanics descriptions over the past decades. One factor contributing to the success of such constitutive laws is that in compression, high isotropic pressure loading represents a small strain process due to strong interatomic potential resisting motion. However, in shear and tension, large strain effects can nucleate at defects in the material structure. Thus more realistic modelling must take fuller account of the structures of the material at various length scales. For metals this requires an understanding of the initial metallurgy or material production and thereafter the materials science during processing which first develops the microstructure before its second evolution during mechanical loading.

Metals

A full treatment of the response of all metal microstructures and alloying effects is a large task since the questions posed by experiment are still, in many cases, a work in progress. Further, the full analytical description of the processes identified with numerical implementation into continuum design codes has not as yet been fully completed and thus a multiscale attempt to fully model operating processes from first principals is the subject of another review in itself. Rather it is the intention of this article to elaborate the experimentally observed shock response of three metals of differing structures to illustrate some of the recent advances in understanding when metals are subject to shock, the most rapid of all loading. The materials chosen are pure nickel (face-centred cubic; FCC), pure tantalum (body-centred cubic; BCC) and the titanium alloy, Ti–6Al–4V that although a two phase material, has deformation dominated by the α phase (hexagonal-close-packed; HCP). Additionally, intermetallics with simple structures are also discussed including the behaviour of the ordered FCC material Ni_3Al (possessing the $L1_2$ structure type) and of the face-centred tetragonal; FCT ($L1_0$) material based on the intermetallic compound, TiAl. Here, the research is much less extensive, and work has been largely conducted on materials based upon the composition, Ti–48at%Al, which means the alloys contain a small, yet significant amount of the $D0_{19}$ ordered hexagonal phase Ti_3Al. These materials are used as examples to illustrate the response of a much wider community of metals and alloys with similar microstructures under shock loading. The compositions and the quasi-static properties of the metals are given in a series of tables and these are collated for completeness into an appendix at the end of the review.

As a pure FCC metal, the response of nickel under shock has received a high level of attention. The effect of prior cold work (through rolling) was investigated by Rose et al. [40]. Upon recovery from shock loading, the hardness was

noted to reach a near-constant level, regardless of the level of prior work. It was suggested that this was due to shock hardening being controlled by dislocation motion and generation, with twin formation and stacking faults having an insignificant effect. In contrast, Kressel and Brown [41] showed that dislocation and point defect concentration increased eightfold (compared to a cold rolled sample at 0 °C) when rolled to the same equivalent strain. Similar results in nickel and copper were demonstrated by Grace [42]. Focusing on the microstructure, Murr and Kuhlmann-Wilsdorf [43] showed that shock-loaded nickel deformed via dislocation motion and generation, forming into dislocation cells as seen in the recovered samples. At an impact stress of ca. 25 GPa, dislocation cell size was observed to be near constant with increasing pulse duration, but the deformation structure did not reach a steady state until approximately 0.5 μs, indicating that the shock response of nickel (and presumably other materials) has a degree of time dependence. These results were consistent with the later work of Wright and Mikkola [44] on copper germanium alloys when shocked with short duration pulses. In contrast, shock amplitude was shown to have an effect, with cell size being inversely proportional to stress amplitude. Greulich and Murr [45] showed that the initial microstructure, in terms of grain size and orientation, had little effect upon the shocked microstructure. The most thorough microstructural investigation on shock loaded nickel was by Follansbee and Gray [23] who used momentum traps to prevent lateral releases affecting the final microstructure [46]. They investigated two polycrystalline grain sizes (40 and 225 μm) and two single crystal orientations ($\langle 111 \rangle$ and $\langle 100 \rangle$). The recovered microstructures showed the same features as discussed by the previous authors. Compared on a resolved shear stress basis, little difference was observed in the shock-induced hardening between either grain size or crystallographic orientation, although the dislocation cell size was noted to be smaller in the single crystals. Finally, Meyers et al. [47] investigated the effects of temperature (77 and 300 K) on the shock-induced microstructure of nickel, with the cell formation at the lower temperature being less well defined than at higher temperatures. They also indicated that cell size was pulse duration dependent, but given previous results from other authors [48], they conceded that this may have been due to inadequate momentum trapping.

The response of tantalum under shock loading conditions has also received a degree of attention as a model BCC metal and as it has application within the conventional ordnance community. A body of work has investigated the Hugoniot, see for example the works of Walsh et al. [49], and Rohde and Towne [50] who examined the material at stresses in excess of 25 GPa. Stresses below 12 GPa were examined more recently by Furnish et al. [51], whilst Mitchell and Nellis [52] extended the Hugoniot to above 400 GPa. A discrepancy between experimental and modelled data of the arrival of the elastic and plastic waves was explained by Furnish et al. [53] in terms of material anisotropy. Fiske et al. [54], in observing similar results, suggested that this may alternatively be due to a non-linear $U_S - u_p$ relationship in the weak shock regime.

Under low shock stresses (below 20 GPa), the mechanical response is driven by microstructual development. Gray and Vecchio [55] shock loaded and recovered tantalum following shock prestraining at 7 and 20 GPa, using full momentum trapping techniques to minimize as much as possible the interaction of lateral releases affecting the recovered microstructure [56]. Results showed that deformation occurred by the motion of long, straight, screw dislocations of system $a/2\langle 111 \rangle \{110\}$. The total dislocation density was observed to increase slowly, consistent with a high Peierls stress favouring the motion of existing dislocations rather than the formation of new ones. Post-shock mechanical testing revealed that no significant post-shock hardening occurred reflected in the observed microstructural development, in contrast to that shown by nickel. Repeated experiments carried out at 218 and 410 °C did show enhanced hardening (compared to those at lower temperatures). It was suggested that this was due to a combination of strain aging and enhanced dislocation storage tied to thermally activated processes such as cross-slip. At much higher stresses (45 GPa), Murr et al. [57] noted that shockwave deformation also occurred via contributions from twinning. Hsiung and Lassila [58], also shocking Ta to 45 GPa observed, in addition to twins of type $\{112\}$, evidence of a BCC (β) to hexagonal (ω) phase transformation. The orientation relationships between the two phases were determined to be $\{10\bar{1}0\}\omega$ parallel to $\{211\}\beta$ and $\{0001\}\omega$ parallel to $[0\bar{1}1]\beta$.

The intermetallic compound, Ni_3Al, possesses an ordered FCC lattice, based upon the Cu_3Au, $L1_2$ structural prototype. Interest in this material has been driven from two areas. Firstly, under quasi-static conditions, the material has a positive dependence of strength with temperature, up to ca. 700 °C. This has been ascribed to the Kier–Wilsdorf [59] locking mechanism. Here, mobile dislocations of Burger's vector $\langle 110 \rangle$ on $\{111\}$ planes, cross slip on to the cube $\{100\}$ planes, where they are sessile. As this is a thermally activated process, it will become more prevalent as temperature increases, until sufficient thermal activation allows movement on the $\{100\}$ planes. At higher strain-rates (ca. 8000 s^{-1}), Sizek and Gray [60], showed the same mechanisms in operation. However, flow stresses did not reach a maximum at 700 °C, but continued to rise, possibly due to the suppression of dynamic recovery by the high imposed strain-rates. Experiments conducted under one-dimensional shock loading by Gray [61] showed that

Ni_3Al showed significant post-shock hardening, similar to pure nickel. Further microstructural analysis via transmission electron microscopy (TEM) revealed the major deformation mechanism to be planar slip on the {111} planes, but with a significant contribution of twinning (also on {111}) with an assumed twin direction of ⟨112⟩ [62].

A single crystal alloy, consisting of 90 vol.% Ni_3Al, was shocked up to 100 GPa by Kasantseva et al. [63], with results indicating that there was a phase transformation from the cubic $L1_2$ to the tetragonal $D0_{22}$ phase. It has also been suggested [64] that there is an order–disorder transformation at ca. 205 GPa.

The intermetallic compound TiAl has attracted attention from the aerospace community as an alternative to existing jet turbine materials in some applications, as it offers significant reductions in density and increases in temperature performance. Alternating layers of titanium and aluminium atoms lie on the (200) planes, resulting in a face-centred tetragonal (FCT) L_{10} structural prototype with a *c*/*a* ratio of ca. 1.03 [65]. Although the structure is near cubic, the differences in atomic configuration in the different axes (Ti–Al–Ti in the *c* axis and either Al–Al–Al or Ti–Ti–Ti in the *a* axis) gives a large reduction in the symmetry and hence the ability to plastically deform when compared to higher symmetry cubic systems, such as those described above. In the single phase material, deformation occurs either via normal dislocations of type ½⟨110], or super dislocations of type ⟨011] or ½⟨112], all on the {111} planes. Mobility is limited at room temperature, in the case of normal dislocations due to a large Peierls stress due to anisotropy of charge density around titanium atoms. However, the low toughness of single phase compositions, has led to alloy developments where a reduction of aluminium content results in the formation of the hexagonal Ti_3Al α_2 phase. In compositions in the range Ti–47–50Al, deformation was observed to occur via normal dislocation motion and generation, with twinning also occurring. However, the precise nature of deformation, and hence mechanical properties, is affected by the nature of the microstructure, which can be manipulated through heat treatment and thermo-mechanical working.

Existing data from high strain-rate experiments on these intermetallics is more scarce. Maloy and Gray [66] investigated a two phase material based upon the composition, Ti–48Al–2Cr–2Nb, using a split Hopkinson pressure bar (SHPB) at a strain-rate of ca. 2000 s^{-1}. At 5% strain, they noted a stress of 800 MPa at 25 °C, dropping to 550 MPa at 600 °C before increasing again to 700 MPa at 1100 °C. Gardiner et al. [67] made similar observations. Further, both groups also noted very high work hardening rates, with the former observing a near twofold increase at 25 °C as strain-rate increased from 0.001 to 2000 s^{-1}. Under one-dimensional shock loading conditions, Gray [68] recovered Ti48Al–2Cr–2Nb using full lateral momentum trapping techniques [56]. At 10 GPa, the shocked microstructure was shown to consist of dislocations slipping on the a/2⟨110}{111}system, with some deformation also accommodated by ⟨112⟩{111} twinning. Post-shock mechanical properties showed no additional strengthening when compared to quasi-static deformation, when taking the equivalent shock strain into account.

The common titanium-based engineering alloy, Ti–6Al–4V (constituents in weight%, referred hence forth as Ti64) is generally supplied as a two phase material. The majority α phase (hexagonal-close-packed; HCP) exists as a network of grains, with an infill of transformed β (body-centred cubic) phase between them, with a small amount untransformed. As a consequence, deformation is dominated by the α phase, with the preferred slip system consisting of $\frac{1}{3}\langle 11\bar{2}0\rangle$ dislocations on the basal (0001) planes. Slip can also occur on the prismatic $\{1\bar{1}00\}$ and pyramidal $\{1\bar{1}01\}$ planes as well, there being little difference in the critically resolve shear stresses (CRSS) of the various systems [69]. The necessary $c + a$ $\frac{1}{3}\langle 11\bar{2}3\rangle$ dislocation occurs on the $\{1\bar{1}01\}$ planes, but with a much higher CRSS.

The high strain-rate response of Ti64 has attracted attention from the aerospace community, primarily due to its use as a fan blade material in jet turbine engines. As such, it can be subject to events such as bird strike and foreign object damage (FOD). Accordingly, a body of work has investigated simulated FOD events. Peters and Ritchie [70] impacted hardened steel spheres at a velocity of 200–300 m s^{-1} onto flat Ti64 plates, noting that the fatigue resistance dropped significantly, by two orders of magnitude. Thompson et al. [71] made similar observations through the impact of glass spheres onto the leading edge of simulated fan blades. This was attributed to the creation of residual stresses, as the fatigue life was shown to improve by a post-impact annealing treatment. The same authors [72] also noted a reduction of fatigue life as the incident angle of impact increased, although they were unable to systematically correlate the size of the impact crater with fatigue response.

At impact velocities in the range 800–1150 m s^{-1}, of interest to the ballistics community, it has been observed that the microstructure has a major influence on the response of Ti64. Kad and co-workers [73–75] noted that the ballistic performance was essentially constant with increasing annealing temperature, until the β-transus was crossed, whereupon a significant reduction was found. Failure was noted to occur via an adiabatic shear banding mechanism, leading to a 'clean' plug of material of approximately the same diameter as the impactor being removed from the Ti64 target. Below the transus, with the microstructure consisting of grains of the majority HCP α-phase aligned such that the basal planes orientated

towards the long transverse direction of the original rolled plate, shear localization occurred parallel to the rolling direction, and thus cracks were orientated parallel to the surface. In combination with the activation of 'hard' deformation modes in the Ti64, this resulted in the crack energy being dispersed over a much wider area than the previous situation, giving better ballistic performance.

However, the circumstances discussed above generally involve a complex three-dimensional strain state under the impact site, rendering quantitative analysis difficult or even impossible. Simpler loading geometries are necessary if a meaningful analysis of microstructural development and mechanical properties is required. Gray and Morris [76] shock loaded and recovered samples of Ti64, using full lateral release trapping techniques to ensure that the recovered samples were loaded and released under conditions of one-dimensional strain only. Most slip was observed to occur with a Burger's vector of $^1/_3\langle 11\bar{2}0\rangle$, but above a shock stress of 10 GPa, twins of type $\{11\bar{2}1\}$ were also noted. The Hugoniot elastic limit (HEL; yield stress under conditions of one-dimensional strain) has been measured to lie between 2 and 3 GPa [77, 78]. This may be due to variations in oxygen content as Razorenov et al. [79] observed that as oxygen content increased from 0.105 to 0.24 at.%, the HEL increased by 20%, although the dynamic tensile (spall) strength appeared unaffected. However spall strength has been shown by a number of authors [78, 80, 81] to vary with specimen and flyer geometry, increasing as the sample/flyer plate pairs increased in thickness. This led Tyler et al. [81] to suggest that damage formation within the spallation region was time dependent, and hence pulse duration would have a strong influence over tensile behaviour.

Pure titanium has been observed to undergo an α–ω phase transformation during shock loading [82], with the ω phase being morphologically similar to that seen in quenched β-titanium alloys. The transformation lies in the pressure range 2.9–9.0 GPa, depending on purity. However, whether this transformation occurs in Ti64 is open to question. Rosenberg et al. [77] observed a change in slope of the Hugoniot at ca. 10 GPa, but Gray and Morris [76] did not observe any evidence of the ω-phase in recovered samples.

Due to the low symmetry of the HCP unit cell, Ti64 possesses a high degree of anisotropy when processed by conventional hot working techniques. In a very recent article [83], the shock response of Ti64 was analysed in terms of lateral stress and shear strength, parallel to and radially to the long axis of the original as-received bar stock. Textural analysis showed that the material possessed a moderate rod axial $\langle 10\bar{1}0\rangle$ fibre texture, with the c-axis preferentially orientated in the radial direction. Shear strength measurements showed that the material was stronger in the longitudinal direction, although the degree of hardening behind the shock front was greater in the radial direction. It was suggested that this was due to twin formation occurring preferentially in the radial samples in early stages, before $c + a$ slip and dislocation tangling became dominant.

The work discussed in this article will discuss in situ mechanical properties during shock loading (specifically shear strength measurements) in nickel [84], tantalum [85], Ni_3Al [86], TiAl [87] and Ti64 [83] and relate them to detailed microstructural analysis [23, 55, 62, 66] on the same materials. This will be used to illustrate the variety of operating deformation mechanisms and the timescales on which they operate in different classes of metals.

Facilities and techniques

The goal of experimental work is to provide adequate knowledge of the response of the metal over all regimes of the operating mechanisms. By this means, analytical descriptions can be constructed which aim to capture the fundamental relationships between the independent variables, stress and stress state, strain and strain rate and temperature, that independently affect the constitutive, damage and failure behaviour of materials. This includes determining dynamic strength as a function of pressure as well as determining the equation of state of the materials over the range of interest for particular applications.

To develop strength models for metals requires measurement of appropriate mechanical properties. Targets must be loaded in compression, tension, or torsion over a range of loading rates and temperatures appropriate to the application of interest. However, to derive models describing purely material response requires idealized modes of loading which limits the range of techniques available. Such procedures are classified as derivation experiments. In the case of impact loading, testing from quasi-static to shock loading is necessary. A range of mechanical testing frames are available that achieve nominally constant loading rates for limited plastic strains at a constant strain rate. The standard screw-driven or servo-hydraulic testing machines achieve strain rates of up to five per second. Specially designed testing machines, typically equipped with high-capacity servo-hydraulic valves and high-speed control and data acquisition instrumentation, can achieve strain rates as high as 200 per second during compression loading. To achieve higher rates, projectiles are impacted on targets to induce stress-wave propagation in the sample materials. At intermediate strain rate, the principal dynamic loading technique is the split-Hopkinson pressure bar (SHPB) [14], which can achieve the highest uniform uniaxial compressive stress

loading of a specimen at a nominally constant strain rate of about 10^3 per second. It is possible to reach strain rates of up to 2×10^4 per second and true strains of 0.3 in a single test using the SHPB. At these stresses and strain rates, however, the uniformity of stress loading and constancy of strain rate are not guaranteed so that care is necessary. Even with the Hopkinson bar, the use of strain rate to classify the loading become complex. To be strictly accurate, the confined specimen only leaves a state of uniaxial strain when waves can release the central region after travelling across the radius. This takes a small time (microseconds in a pulse length of maybe one hundred microseconds) for fully dense metals but much longer for low wave-speed materials such as highly viscoelastic rubbers or soft high-density metals like lead, so long in fact that the target may not have achieved a uniaxial stress state by the time that the loading pulse has released. Thus the ascription of an average measure such as strain rate becomes complex in wave-dominated problems where the stress state is not stable for a finite time.

Whilst elastic waves displace material that subsequently returns to its original position and density after the front has passed, the shock permanently and irreversibly deforms it into a higher density state. The process occurs so quickly that it is not possible for heat transfer to occur in the time taken for the front to pass. Thus, it is adiabatic and accompanied by a step increase in entropy. At present the suite of experiments capable of generating the shock response in materials of interest consists of a suite of developed methodologies that test response over a pressure range of ca. 1 TPa using impulses ranging from quasi-static high pressure cells to nanosecond pulsed-laser sources. A schematic of the range of devices and their operational regimes is illustrated in Fig. 1. The loading represented is mode I and reflects the final temperature achieved in the test as a colour, with blue representing the isothermal state (ambient temperature) and red the adiabatic (shock temperature) achieved using the relevant methodology. To populate the relevant material descriptions for all components of a device requires models that cover this entire three-dimensional space with validated certainty. At present it is only possible to load for nanosecond pulse lengths over a small target size to the highest pressures. This limits the mechanisms and microstructures that can be probed with such tests. As the compression amplitude decreases, it is easier to apply long pulses to microstructures representative of the continuum until, under ambient conditions, the diamond anvil cell provides high loading pressures but only over a sample dimension of order 1 μm at these high values.

The condensed phase (for most materials) defines a pressure and temperature range of interest which may be approximately fixed at less than a TPa and less than

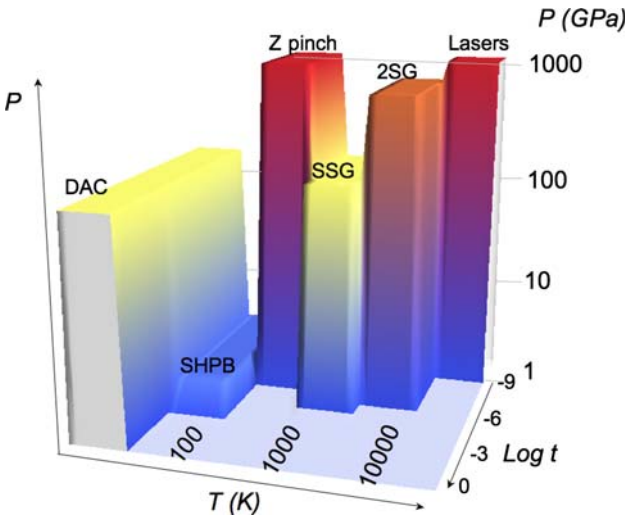

Fig. 1 Loading equipment and delivered impulse covering commonly used methodologies. *P* is the maximum pressure achieved in the loading, *t* the pulse duration of the technique applied and *T* the temperature achieved in the pulse. SSG and 2SG are single and two stage guns respectively, SHPB is the Split Hopkinson pressure bar and DAC the diamond anvil cell. The colour (blue to red) indicates the temperature achieved in loading at the highest amplitudes

10,000 K respectively. There are four principle groups of loading technique employed to recover material response over this regime, three of which are dynamic and including: laser-induced plasma loading, Z pinch devices, compressed gas and powder-driven launchers and energetic drives, and diamond anvil cells (DACs). The laser methods introduce short pulses (typically less than a few ns) yet the largest can apply the highest pressures (TPa) and heat adiabatically to high temperature if a shock is launched. They ablate a plasma on the surface of a target which pressurizes a face. The loading pulse applied is spatially and temporally difficult to control and this limits the impulse applied. The optical challenges of high power lasers fix the focused spots to be small which means that they are unable to apply spatially uniform illumination across a large target area. They are consequently limited at present to probing subgrain dimensions and this limits the mechanisms that can be excited and probed. Thus they are used to investigate the early time, shocked state of a material probing sub-grain length scales. Recent developments have reflected X-rays at the plasma/solid interface to recover the unit cell conformation under high pressures [88]. Nevertheless, new facilities have been built over the last decade and if matched diagnostics and analysis techniques can follow the possibilities for studying early time properties of perfect crystals to extremes of pressure are exciting. Z pinch devices can provide pulses of hundreds of nanoseconds duration and can thus load targets of hundreds of microns dimension. They also have the capability to

allow stress to increase over a similar time period limiting temperature rise and leading to (at worst) a quasi-isentropic loading path. They also have the ability to launch plates that can shock targets rather then employing direct magnetic interactions to apply the loading more slowly. The technology is becoming increasingly mature and the technique is being actively worked on in the laboratories possessing the machines [29].

Gas and powder-driven launchers are capable of loading samples of size and for duration limited by the dimensions of the device. The stresses they can achieve are limited by the propulsion method adopted, but typically they can shock-load materials to hundreds of GPa for tens of microseconds over sample volumes of cm^3. They are precision devices providing well-defined loading impulse over times relevant to all the operating plasticity mechanisms which enables kinetics to be deduced from the response to the loading. Since they are a mature technique the analysis is equally pedigreed. The innovations in this technology are principally in the development, use and linkage to analysis of new diagnostics.

Diamond anvil cells (DACs) have been used since the time of Bridgman to compress materials hydrostatically to hundreds of GPa [89]. Clearly they can access impressive pressure ranges within a material but the size of the cell limits the loading to single crystal targets that at the highest pressures are only of micron dimensions. Also the timescales over which they load are orders of magnitude slower than those in the dynamic cases discussed above, meaning that pathways with different kinetics may operate in diamond anvil cells than are observed under shock loading. Thus, whilst the DAC accesses equilibrium states, the dynamic case frequently jumps via metastable ones at differing thresholds in state variables. New challenges are pushing the cells and the pressure sensing methods to ever-higher pressures. Beyond 100 GPa there is a limitation in assuring the stress sate in the target and to sense pressure with great accuracy. This represents work in progress for the technique but the advent of ever-brighter light sources has opened new possibilities for interrogating structure for the field [90].

A series of pressure-induced deformation mechanisms, each with different respective kinetics is triggered by shock acceleration of the impact face of the material. Figure 2 shows the pressure–time plane of the plot of Fig. 1 with colour coding for the temperature (red, adiabatic; blue; isothermal). The various operating regimes for the devices are dimmed so that a series of representative times for some important plasticity mechanisms in shocked metals might be superposed at times representing the order of magnitude for their kinetics. Such a cross-plot gives more information about a suite of experiments than might first be appreciated. For instance, spallation, the dynamic tensile

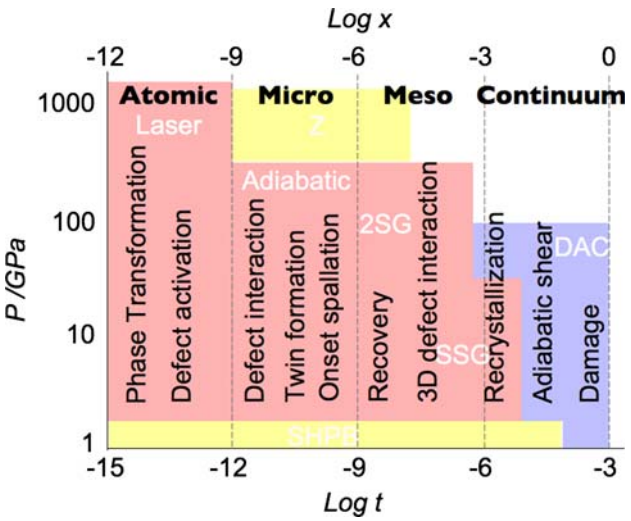

Fig. 2 Operating metal deformation and damage mechanisms and their characteristic length scales and time scales. Time scales along the ordinate map to length scales along the top through the wave speed in the material (which is of order 1000 m s^{-1} in metals). Thus a pulse of 1 μs sweeps and loads a spatial dimension of 1 mm

failure of the metal, often operates by nucleating and growing voids within the material. These preferentially grow from defect sites activated by tensile reflections and are of order 1 μm in dimension. This places a lower limit on the time required to activate such a volume of around 1 ns which explains why measures of tensile strength using laser pulse interactions yield values much higher than devices that apply longer loading. A short pulse length will not access the full extent of the distribution of defects or the representative microstructure within the material so that it will appear to display a higher strength than the continuum. This pulse-dependent response is equivalent to the sample-size effects well established in the fracture toughness community. The connection between time- and length scales may be approximated through a wave speed for the material as the measure of communication of information through the microstructure. Without the complication of considering a particular material, a representative wave speed of 1000 m s^{-1} is assumed being of the correct order of magnitude to rank response.

The moment of impact or the application of a pressure pulse onto the surface defines the onset of impulsive loading in a solid. At that moment the first plane of atoms on that surface is accelerated inwards and the interatomic potentials provide an elastic response in the material to the insult. It is only after a characteristic time that the microstructure can respond in some manner to this step load and it is the range of these processes and their kinetics that occupies what follows.

The fastest mechanisms by which a lattice can respond include phase transformations, the activation of dislocation

activity and twin formation which can all occur within the first nanosecond after the shock is applied although experimental kinetic information in this regime is very limited [88]. The most powerful lasers match these loading times and so can potentially yield information on these mechanisms on their micron dimension targets (although clearly other shock devices are also relevant if a sensor can be placed close enough to the impact face). One of the responses that is possible in many metals is for the unit cell to reorient to a denser form via a solid–solid phase transformation. All indications are that this process is extremely fast. However continuum measurements of transformation stress thresholds show that the process always occurs after the plastic wave has passed indicating the defect relaxation of the microstructure is necessary to trigger the process. Another process of relevance is the relaxation of the elastic state by activation of defects that allows slip to attain a plastic state behind the front. This is the first of the many processes discussed in what is to follow that depends upon the statistics of the defect population that exists in the target before loading. It will be become apparent that different physical approaches are necessary to appreciate results coming from experiments probing the atomic scale than are required for those that interrogate the mesoscale. A final rapid mechanism that probably proceeds somewhat slower than the two above is twinning as it requires partial dislocation nucleation and motion to produce the twins. In all of these cases, accurate measurement of deformation at these length scales and time scales is difficult and techniques are under development at the present time to address this need. The possibility of imaging with ever-brighter light sources over the next decade offers the promise of observing some of these effects and their kinetics for the first time.

To access mechanisms that require the activated dislocations to propagate and interact with each other and subsequently boundaries, requires hundreds of nanoseconds or microseconds. Further, targets that can host pulses of this length are of a minimum dimension of around a hundred microns that means that they will always contain defects. Such timescales and length scales are required if hardening and the onset of localization processes which lead to spallation are to be captured. To investigate processes such as fracture, recrystallization or adiabatic shear therefore requires times of around 10 μs and targets of tens of mm so that only larger launchers or HE-drive can apply the required impulse to excite these mechanisms. Finally, processes such as full-target failure require longer timescales again to connect damage nucleation sites and open a failure surface.

It is useful to classify the loading regimes described above into four groupings based on the length scales considered. Engineering design at laboratory scales requires experiment and modelling applicable to the continuum. To focus down to microstructural length scales on the other hand requires one to probe a scale where bulk inhomogeneities are understood and their role in continuum mechanisms is assessed and then quantitatively addressed. This microstructural length scale is dubbed the mesoscale. At a length scale beneath this again is the microscale, where the microstructural features addressed are recognized as groupings of atoms to study processes such as slip and twinning. Finally the atomic scale accesses the physics that results from interactions occurring within the unit cell. By this means one can say that laser techniques access the atomic scale, launchers (Z pinch, gun or HE) are necessary to access the micro- and mesoscale, whilst Hopkinson bars or load frames test the continuum. The device that flaunts this classification is the DAC, where the long loading time is not matched to the dimension of the target it interrogates. Here it is this that determines that the technique focuses upon atomic scale phenomena.

Comparing devices to host investigation of the spectrum of deformation and damage evolution processes of interest is a complex task when considered in isolation from the applications to which they are relevant. What is more useful is to view all available experimental techniques from the standpoint of a community with a perceived need. At the present time, a primary requirement is to identify the mechanisms necessary to populate the modelling and simulation environments required to support design activities. By these standards, each can be judged as to its success in achieving a description of material performance over the operational range picked for condensed matter physics above. From this perspective, lasers and DACs load small volumes of material and probe the unit cell or nanometric substructure, whereas launchers and Z pinch machines investigate continuum dimensions by virtue of the larger target volumes and therefore microstructural scales interrogated. Whilst techniques that load a material using shockwave loading do so adiabatically, shock-less techniques have the capability to take compression to lower temperatures so achieving higher-pressure states more easily in the laboratory. On the other hand, laser techniques can load at the highest pressures, yet the loading times are so small that the plastic state is barely achieved. Only launchers or HE lenses can load for the tens of microseconds required for localization to occur to form shear bands. Thus for a general need to populate materials descriptions over a wider operating range and for describing the bulk response of materials, all of these devices and both in situ and post-mortem techniques are required to resolve the temporally and spatially non-equilibrium response of materials in extreme environments.

In the shock regime (up to a few hundred GPa) where one is studying primarily the condensed state, loading has

been applied in a configuration where the material is subjected to a state of uniaxial strain at the continuum. In this regime a planar shock wave is introduced into a target by the impact of a flat plate from a gas-driven launcher with precise alignment of impactor and target prepared to high tolerance. This technique is often dubbed plate impact and it is this geometry that will be used to apply shock pulses to the metals considered in what follows. Applications accessing stress levels induced by direct contact from a detonating high explosive, through blast and down to other lower amplitude impulsive loadings occupy this regime. The response of metals here is dominated by thermally activated dislocation motion as a primary plasticity mechanism and this will be followed through subsequent sections. At higher levels the deformation is controlled by dislocation drag and this regime will be mentioned but not further developed here.

Shock experiments

Sensors and experimental geometries

A plate impact experiment delivers a well-defined and experimentally measurable pulse into the stationary target that allows tracking of material properties. On the impact face, the pulse is square with a duration determined by twice the flyer thickness divided by the appropriate wave speeds. As the pulse progresses through the target the elastic wave travels faster than the plastic so that dispersion occurs and a step develops. Driven waves in most materials steepen as they travel since the sound speed increases with pressure. Conversely this means that waves relieving pressure (dubbed fans) disperse, since the head of the release travel faster than the tail. An exception occurs in materials that change phase (solid–solid phase transition) where releases can steepen into shocks but the metals considered here do not in the regimes considered. A representation of a one-dimensional impact is a distance-time, X–t diagram shown in Fig. 3. The position of a stress sensor is indicated by the vertical line at 2 mm. A representation of the longitudinal stress pulse induced in the target at the position indicated is shown in the figure and key features are discussed in what follows. At this time the elastic precursor precedes the plastic front and the releases show a rapid elastic, and then a slower plastic component.

Any impact drives particles ahead of the impactor at a characteristic particle velocity, u_p, into material of initial density ρ_0. The shock at the head of this wave travels at a characteristic shock velocity U_s and pressure P and is compressed to density ρ_1. Conservation of mass and momentum yield the relations

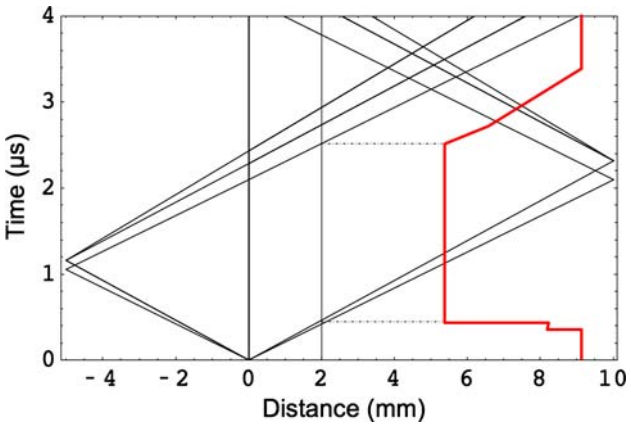

Fig. 3 Lagrangian representation of a shock experiment; X–t diagram. Impact is at $t = 0$ and elastic and plastic shocks travel into flyer plate (left; $x < 0$) and target to the right ($x > 0$). Reflection leads to elastic and plastic releases which form a fan since $c(p)$. The line at 2 mm represents a sensor location and the red curve a stress history at that point (stress horizontal rising the left) and time running vertical with the axis. Representation is for 5 mm thick copper flyer plate impact 10 mm thick copper target at 500 m s^{-1}

$$\rho_0 U_s = \rho_1 (U_s - u_p), \text{ conservation of mass,} \tag{5}$$

and

$$P = \rho_0 U_s u_p, \text{ conservation of momentum.} \tag{6}$$

For most materials tested (that do not alter their phase during loading) the relationship between the shock velocity achieved for a particular input driving velocity is linear, that is to say U_s is related via two constants, c_0 and S, to u_p thus

$$U_s = c_0 + S u_p. \tag{7}$$

The curve that defines the shock states achieved by a material (which is called the Hugoniot) exhibits a simpler related counterpart called a hydrodynamic curve for a material recovered by substituting 7 into 6 to give a quadratic relation between P and u_p. The measured values of the shock parameters are shown in Table 6 in the Appendix.

$$P = \rho_0 (c_0 + S u_p) u_p. \tag{8}$$

Using these values, and the constants from the above curves for the five metals, the hydrodynamic response can be plotted along with experimental points recovered from experiments similar to those discussed above.

Sensors must be chosen to measure features of the shocked flow in a material. One approach is to observe free surfaces with interferometry and deduce the velocity history [92]. A second is to embed piezoresistive sensors into the flow to record components of the local stress or strain [93]. Sensors must be embedded within sectioned targets and be of finite dimension. Thus their response time and

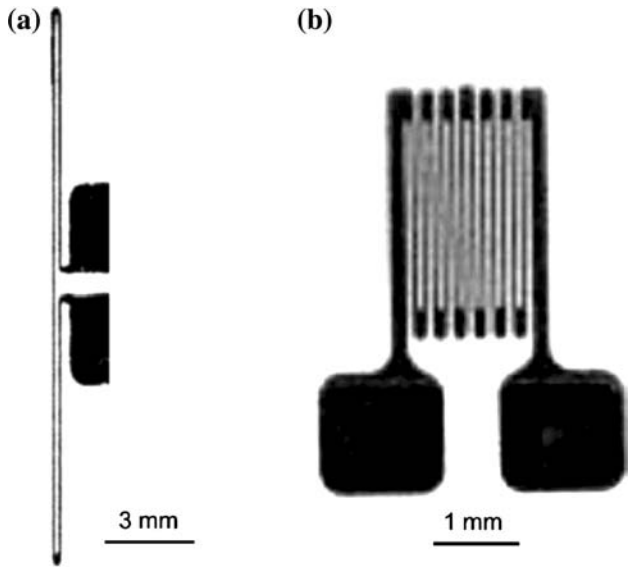

Fig. 4 Two common geometries for micromeasurements manganin piezoresistive stress gauges [91]. **a** T-shaped (MicroMeasurements J2M-SS-580SF-025 of 25 Ω) and **b** grid (MicroMeasurements C-951213-C) forms of resistance 48 Ω

sampling area are both finite; this must be taken into account when interpreting their response. Two embedded manganin stress sensors used in this work are shown in Fig. 4. The gauges were of differing initial resistance, and had T-shaped (MicroMeasurements J2M-SS-580SF-025 of 25 Ω), and grid (MicroMeasurements C-951213-C and LM-SS-025CH-048) forms of resistance 48 Ω. When placed in a plane perpendicular to that of the shock, the wave sweeps across an active region of dimension 240 μm for the T gauge, which extends over 15 mm (Fig. 4a). Figure 4b shows a small grid gauge, C-951213-C, which has an active element of width 1 mm. In other experiments, the grid gauge LM-SS-025CH-048 was used with a swept width under shock load of 5 mm. In both cases the sensors were etched on a glass fibre backing and the manganin foil was then of 5 μm thickness. In the following, the two will be referred to as 'T' and 'grid' gauges, respectively. The grid gauge was embedded between target tiles and used to sense the longitudinal stress pulse passing the gauge location. The fastest response time is 20 ns in this configuration since the shock only sweeps the thickness of the foil. The T-gauge was used to measure the lateral stress component and was mounted in a cut at 90° to the plane of the shock between insulating sheets and of width ca. 100 μm. The shock must sweep the full gauge and equilibrate with the stress field before the gauge can be equilibrated. This process takes ca. 200 ns. Details of the calibration of these sensors and of the various gauge mounting and responses are given in Ref. [91]. Embedding sensors is the only means of directly recording stress histories at a point in the flow within a material.

For an isotropic material, uniaxial strain imposed globally allows only two orthogonal components of the axisymmetric stress field and measurement of both at a point allows direct deduction of the shear stress development at the same longitudinal position using Eq. 3. Such behaviour has been deduced in several ways including the following techniques:

(i) use of the measured stress- and shock velocity versus particle velocity data to construct Hugoniot and hydrodynamic curves (corrected for temperature) to determine their offset and then calculate inferred strength [94],
(ii) employ the pressure-shear technique to directly map the deviatoric behaviour [95],
(iii) allow the release of the material from states induced by single and double shocks to determine by integration the stress offset of the Hugoniot and isentrope [96–99],
(iv) monitor directly the longitudinal (σ_x) and lateral (σ_y) stresses, and assign the difference between the two to the compressive strengths that exist behind the shock front at high pressures [100].

The direct measurement of lateral stresses with piezoresistive gauges has been the focus of intense research over the past 20 years. This has resulted in a more complete understanding of the response of the gauges to various loading conditions in both longitudinal and lateral configurations [91, 101–106]. The indirect methods of determining strength cannot provide a continuous strength history so that measurement of longitudinal and lateral stresses with appropriate sensors is preferred here.

Figure 5 shows a typical target configuration used in the experiment described below. Two gauges, measuring longitudinal stress and separated by a known distance d used to measure the development of the pulse and the time of travel of the shock between each Lagrangian location, are shown in Fig. 5a. By this means, a value for U_s can be obtained. Also the development of stress thresholds such as the HEL can be monitored. One of the phenomena frequently observed in experiment is the decay of the elastic precursor magnitude with distance into a target. This phenomenon is known as precursor decay and is observed in many metals. This will be returned to later in regard to the materials chosen for comment in the results section.

In other experiments, a T gauge was mounted a known distance from the impact face in a target reassembled from two tiles with a gauge mounted between. The geometrical arrangement for this is shown in Fig. 5b. In some cases two gauges could be mounted into the target to see wave development at a particular stress level.

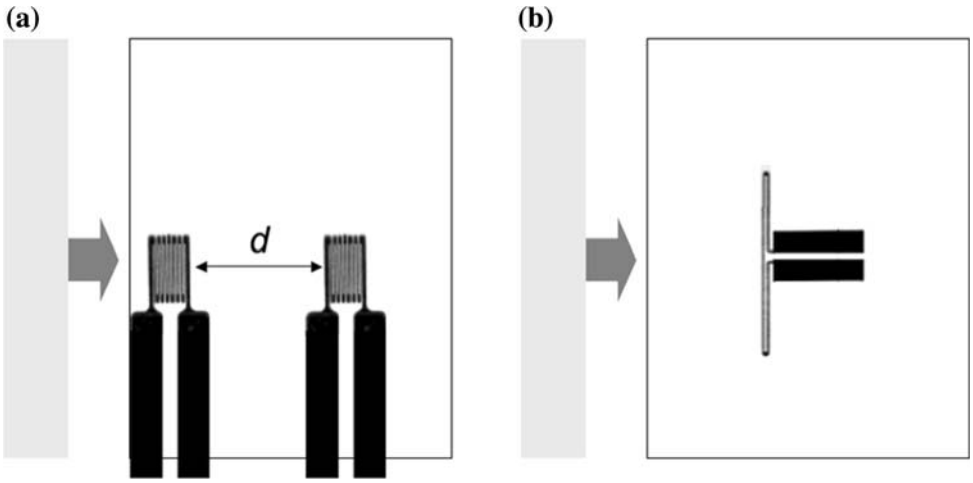

Fig. 5 Schematic experimental configuration used. **a** Two longitudinal gauges placed at known separation *d* in the longitudinal orientation. **b** Lateral gauge placed 4 mm from the impact face

Recovery experiments

To observe details of the evolution of a microstructure in a material requires a means of isolating it in a precisely known loading state. To do so requires varying means of trapping the lateral, late-time momentum due to radial release waves and different devices to introduce the shock-loading pulse [110–119]. To reach a working target configuration requires detailed design to optimize target geometry [120–125]. One method of soft shock-recovery, designed for use on gas/powder launchers, has successfully demonstrated the ability to reproducibly yield recovered samples possessing low residual plastic strains and has been widely adopted [111, 126–128]. A key need is to trap radial release waves coming in from the external surfaces of the target. To do so requires momentum trapping rings around its centre which contain the radial releases before they may enter the sample to be examined [126, 128]. Additionally good lubrication and accurate target preparation, assembly tolerances and surface finishes are required to produce samples with residual strains of <2% [128–130].

Of course, the targets must also be decelerated in a prescribed manner to avoid further plastic deformation and thereafter, the induced shock temperature rise must be rapidly dissipated, before the microstructural defects, generated and stored in the sample due to the shock-loading excursion, are significantly altered by thermally driven relaxation/static recovery [126, 128]. This later thermal management is generally achieved by plunging the central portion of the shock-recovery assembly into a liquid bath immediately after the shock has released [110, 118, 119, 126].

Simulations using pedigree materials' models to optimize the best geometry for the one-dimensional shock and recovery of samples subject to a defined 1D shock compression and release pulse and an example of the behaviour of the target, are shown in Fig. 6 [107]. This simulation

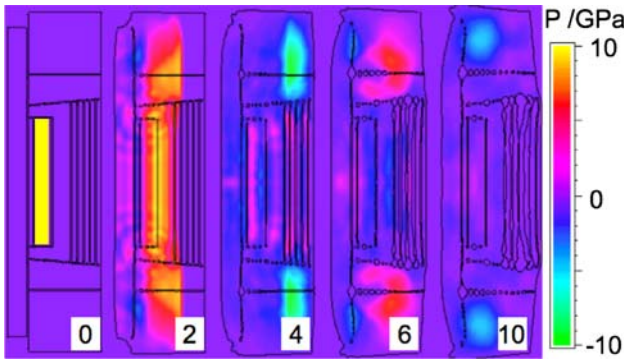

Fig. 6 Impact of copper impactor onto a copper target at 500 m s^{-1}. The simulation shows a copper flyer impacting the baseline recovery assembly. The colour levels show pressure in the assembly as a function of position in the assembly. The yellow segment in the 0 μs frame marks the initial configuration of the sample recovered for examination. The times after impact of each frame are in μs [107–109]

shows a slice through a target during the impact of a flyer plate to the left onto a target to the right, which is sectioned into outer confining rings and an inner section in which only the sample disc (rectangle in the simulation) shaded yellow in the first frame is recovered. The figures by each frame are the time after impact that each represents. Two microseconds after impact, a pulse (around 9 GPa so orange) has travelled into the target and is sweeping across the sample. By 4 μs it has traversed the target and reflected creating a tensile pulse (green). This has the effect of pulling apart a series of plates trapping the tensile part of the pulse that would otherwise enter the sample. Equally lateral rings trap unloading from the edges that would ordinarily take the target into three-dimensional strain after the shock has passed. The snapshots at 6 and 10 μs show the wave bouncing in these rings changing phase from compression to tension as it does so but the region in the sample area remaining in 1D strain. The details of the simulation and other features of the loading are give in

Ref. [107]. Clearly there remains deceleration of the target, cooling of the sample and the deceleration of subsidiary components that could additionally load the sample, but these effects are assumed to be of lesser importance since the loads applied will be small in comparison to those considered here.

The soft recovery of shock-loaded materials is proving of increasing importance in the understanding of material response subjected to impulsive loading. It is anticipated that efforts such as this applied to other classes of material will reveal details of their response that will open up new areas of research.

Results

As discussed above, five materials were selected in this review to illustrate metallic response to shockwave loading. These were FCC nickel, the ordered FCC intermetallic Ni_3Al, the BCC metal tantalum, two alloys based on the intermetallic phase TiAl (Ti–46.5Al–2Cr–2Nb and Ti–48Al–2Cr–2Nb–1B) and Ti–6Al–4V that is composed primarily of the HCP α-phase.

Shock loading provides a probe to excite and differentiate between a number of operating deformation mechanisms in the compression response of materials. As microstructure restricts the available slip systems and as atomic bonding becomes stronger, the evolution of the strength of a material changes under dynamic loading.

Longitudinal stress histories in the metals under consideration are presented in Fig. 7. The traces were recorded with a sensor backed by a PMMA block to the rear of the target that allows the gauge to respond quickly with an optimal equilibration time (limiting the rise time recordable) of ca. 20 ns. The pulses were recorded at positions that allow the elastic and plastic fronts to disperse as described above. A longitudinal stress measured in the PMMA can be converted to that of the original compression in the target using impedance matching at the interface. The impacts were at a stress at least five times the HEL of the metal in question in order that the processes of defect generation and storage were driven at their maximum rate. From such histories it is possible to infer the maximum stress achieved at different impact speeds that allows one to deduce the thermodynamic equation of state of the material. This data determine the hydrodynamic response of the material to shock since it defines the thermodynamic states accessed. Two other features of the pulse are significant: firstly the rate of rise of the plastic part of the wave, and secondly the roll over time taken for it to reach the peak stress plateau value from this steady rise.

The pure FCC and BCC metals Ni and Ta show that the rise of the pulse for nickel is an order of magnitude faster

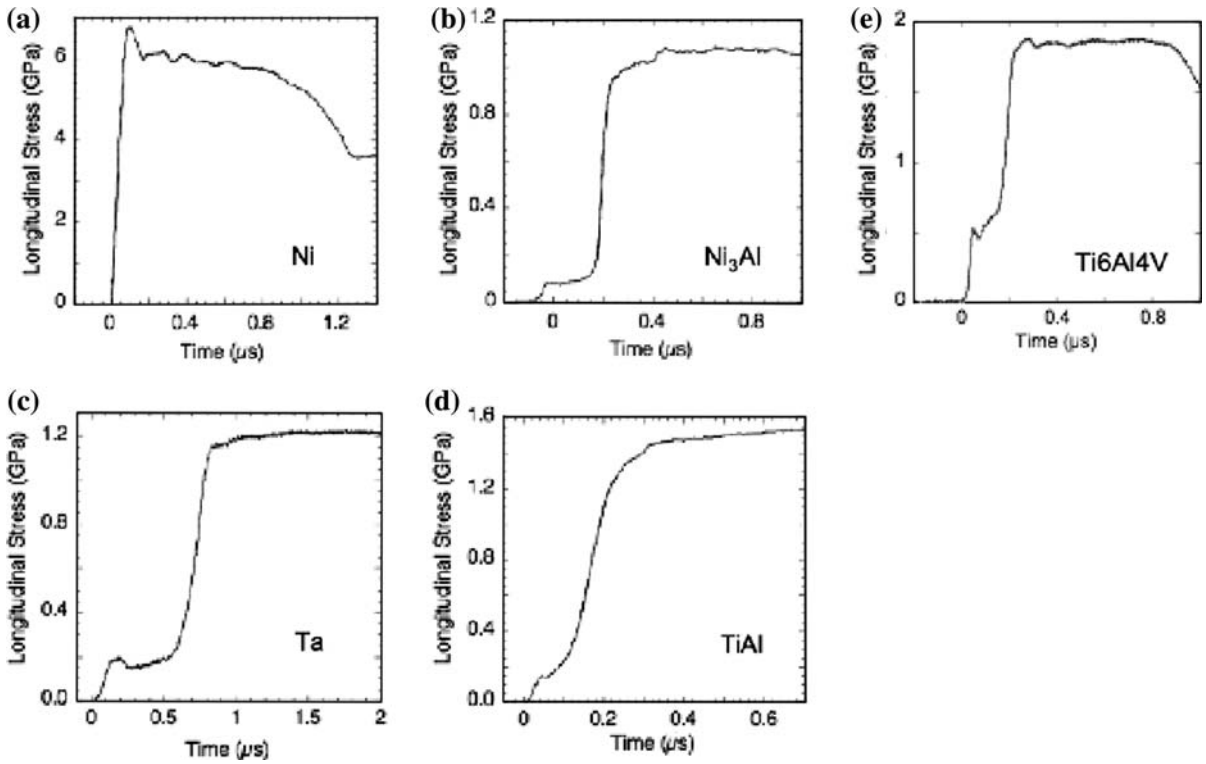

Fig. 7 Backsurface stress wave profiles for the five materials highlighted

than that of tantalum. In fact the pulse in nickel rises faster than the response time of the gauge and causes an overshoot and electrical ringing on the top of the trace that results from the rapid mismatching of the reactive bridge circuit. This contrasts with tantalum where the pulse rises over several hundred nanoseconds and then rolls over, reaching the peak stress more gradually. The plastic wave in Ti64 has a rise time intermediate between that for the two microstructures reflecting the differing features of the slip kinetics in the FCC, HCP and BCC lattices. In contrast, the two intermetallics show similar features, with a fast rise but a slower roll over in the case of Ni_3Al and the slowest rise and longest time to peak stress in the case of TiAl. This will be returned to later in discussions of the global response of these metals.

The traditional means of deducing materials' equations of state (EoS) is to conduct shock physics experiments to measure the principal Hugoniot and then use theory to extrapolate away from these states on the adiabat to others at arbitrary temperature. Viewed in this manner, the Hugoniot is thus a line on an EoS surface describing the locus of states attainable after a material has been shocked. One means of exploring regions of the EoS space away from the Hugoniot, is to adopt a Gruneisen representation of the equation of state surface, accounting for temperature and taking the Hugoniot as a reference curve [39].

For the five metals discussed below, previous work has determined shock parameters and recent experiments have obtained data points. These are plotted in Fig. 8.

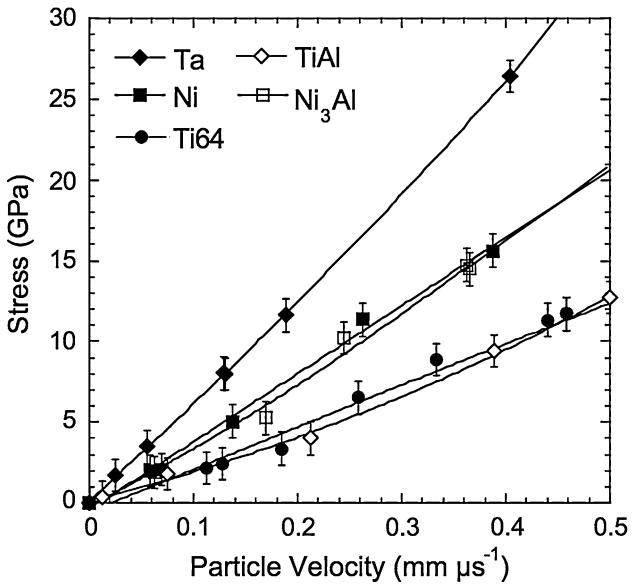

Fig. 8 Hugoniots for the five metals discussed below. The solid curves are taken from the compendium of Marsh [131]. The data points are from experiments conducted on these materials in the work described below

The principal Hugoniots for the five materials are shown in Fig. 8. Experimental points were added from equation of state EoS experiments conducted. The Hugoniots are seen to rank with the elastic impedances of the materials. The lowest of the five is that of TiAl whilst the highest is that for tantalum. These are strongly influenced by the densities of the five metals and alloys considered. The materials tested over the pressure range accessed in the experiments below show no evidence of martensitic transformations [131]. Further there are no transformations visible at higher stresses for these metals in published EoS databases [131, 132]. However, as noted earlier, some workers have reported recovery and identification of a second phase and twinning for polycrystalline tantalum at 45 GPa (ω phase in Ta at 45 GPa) which has not been seen in single crystals [58, 133].

The Hugoniots for nickel and Ni_3Al also show interesting behaviour. The elastic impedance of nickel exceeds that of Ni_3Al such that the Hugoniot for pure Ni is seen to initially lie above that for the alloy. However, beyond a particle velocity of ca. 0.45 mm μs^{-1} this is no longer the case with that for Ni_3Al lying above nickel. This results from the value of S for nickel being larger and thus leading to greater curvature in the Hugoniot. For both the pure materials in this study, S is lower than for the alloys. The curvature of the Hugoniot has been related to changes in bulk modulus with pressure which indicates that the compressibility of the two structures shows differences [39]. The lowest of the five is the curve for TiAl with that for Ti–6Al–4V close, reflecting the respective densities of these materials. The Hugoniot of the material is a measure of the ability of a material to inertially confine the high pressure generated behind the shock front. Thus higher atomic mass and stronger atomistic bonding are reflected in steeper curves in this plane.

Having determined the EoS for the metal, the strength remains an issue that must be addressed in order to construct constitutive models. As discussed previously, monitoring longitudinal and lateral stresses at a location in the axisymmetric stress state behind the shock allows one to determine the shear strength behind the front. In many materials the stress levels follow one another giving a constant strength at a particular pressure. An example is shown in Fig. 9a. In this figure, the longitudinal and lateral stresses and shear strength are shown for the impact of aluminium alloy flyer onto TiAl at 194 m s^{-1}. In the upper, dashed longitudinal stress history the elastic precursor can be seen to precede the plastic front. Since the uniaxial strain impact induces a biaxial stress state, the lateral component of stress acts normal to the impact direction. The shear strength of the material may be reconstructed by taking the difference between the longitudinal and lateral stresses at a Lagrangian station in the target. The histories

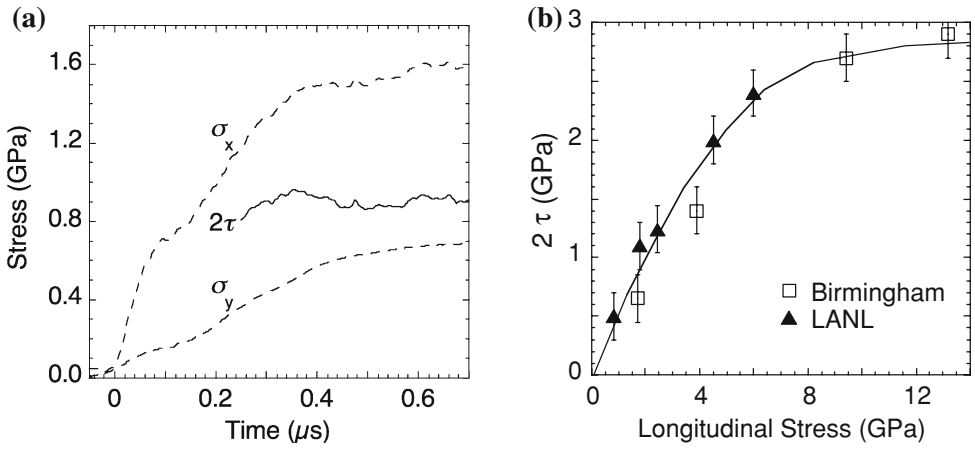

Fig. 9 Shear strength of TiAl **a** Impact of aluminium alloy flyer onto TiAl at 194 m s^{-1}. **b** Strength of two microstructures of the metal at different impact stresses from experiments such as that of (**a**)

presented correspond to one 2 mm from the impact plane in this experiment. The solid curve in Fig. 9a. is generated from the difference in stress between the two pulses corresponding to twice the shear stress (2τ), determined through Eq. 2. Since the sensor has a finite response time, the first 200 ns of the strength curve is not reproduced. Fascinating and as-yet unexplained physics is occurring in this interval; however, at present fast enough gauges to track the development of the state are not available. Rather, new techniques using Z pinch and laser will record events in this short time window.

The longitudinal stress pulse rises first to an elastic stress of ca. 0.8 GPa that corresponds to yield in one-dimensional strain, the Hugoniot elastic limit. There is a second rise to the peak of the pulse over around 100 ns during which dislocation generation, propagation and interaction occurs defining the plastic rise of the pulse. The shear strength is seen to be constant within this plastic rise in this material.

Figure 9b shows the shear strengths of the two TiAl-based alloys considered as a function of the longitudinal stress recorded in a series of experiments like that shown in part (a). There is almost no difference observed between them in the shock even though from quasi-static measurements it might be expected that TiAl1, with its duplex microstructure, would be somewhat stronger than the fully lamellar TiAl2. The materials harden as stress increases but then appear to plateau out above 8 GPa. Most metals show such behaviour in this stress regime. At higher pressures, shock heating is ever greater and it is known that the hydrostatically determined strength drops as the material approaches the melt [134]. However, close to this temperature there is evidence of shock strength increasing again in the work of Kanel and coauthors. They attribute this to creation of vacancies as melt is approached which lock up dislocations in compression yet act as nucleation sites and thus lowering spall strength in tension [135, 136]. This combination of measurements of the stress histories at varying positions to quantify observed behaviour in individual experiments, combined with an overview of the strength at a series of applied stress levels, characterizes the response of the metal. This methodology will be now be used to look at FCC Ni_3Al, the predominantly HCP Ti64 and BCC tantalum under shock.

Figure 10 shows the response of (a) Ni_3Al, (b) Ti64 and (c) tantalum under the impact loads given in the caption to the figure. The global response of the three metals is different with the FCC, the HCP and the BCC microstructures showing differing deviatoric behaviours and kinetics as the yield surface asymptotes to a stable state behind the shock. In the regime chosen for each material, the plastic response is dominated by slip and the key difference in the mechanisms and kinetics are reflected in the shear strength histories shown as solids lines in the figure. FCC materials, show an increasing shear strength in the plastic flow behind the shock [84, 86]. The predominantly HCP Ti64 also displays slight strengthening at early times but then a constant response thereafter like the TiAl in Fig. 9 [83]. BCC metals, at least in a regime where there is minimal activation of deformation twinning, show a softening as seen in the tantalum of Fig. 10c [85, 137, 138].

For the FCC Ni_3Al (Fig. 10a), the lateral stress at the point at which the gauge has equilibrated is seen to be decreasing. On the other hand the longitudinal stress is increasing but more slowly. The strength of the material thus rises over a period of ca. 100 ns over a range of ca. 1 GPa in this case, to a final value for 2τ of 1.5 GPa. The longitudinal stress for Ti64 shows a rapid rise to the HEL and then a slower, rounded ascent in the plastic part of the pulse. The lateral stress shows a slight decrease over the first hundred ns or so but then plateaus out which results in a shear strength which remains constant within the bounds of the electrical ringing on the gauge pulses. In contrast, BCC Ta, shows twice the strength behind the pulse at ca. 4 GPa when the gauges are active, decaying after 1 μs to around 2 GPa. Note here that this reduction in strength

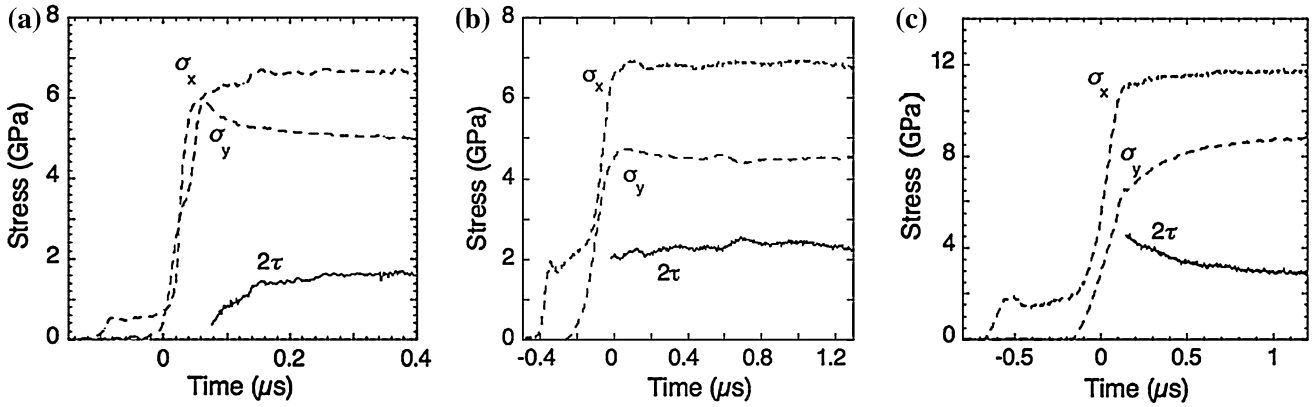

Fig. 10 Longitudinal and lateral stresses and calculated shear stress for impacts onto Ni_3Al and tantalum. **a** Al6082 flyer impacting a Ni_3Al target at 570 m s^{-1}. **b** Ti64 flyer impacting a Ti64 target at 550 m s^{-1}. **c** Copper flyer onto tantalum at 498 m s^{-1}

occurs over a time interval which is an order of magnitude slower for the BCC material then was the case for the rise in strength occurring in the FCC one. This behaviour is mirrored in other pure FCC and BCC materials and indicates the speed of operating dislocation generation and storage mechanisms behind the shock for the two different crystal structures. It is this defect activation and equilibration time which differentiates material classes and leads to differences in the observed dynamic response in continuum experiments.

The strengths of the metals discussed in this review at different stress amplitudes are shown in Fig. 11 so that one of the longitudinal stress amplitudes on the abscissa corresponds to a series of experiments such as those shown in Fig. 10. The initial strengths measured after gauge equilibration behind the shock are displayed as filled diamonds; the open symbol data are measured when the strength has steadied after the shock has passed the gauge station. In the case of Ti64, where the strength is constant during the time of the shock pulse, only the final state (open) symbols are displayed. In the case of the FCC and BCC metals, the shaded region shows the strength developing behind the shock front in a differing manner since the filled diamonds are along the lower strength trajectory in the case of the Ni_3Al and along the higher for the Ta. To show that the yield surface does not develop at a constant rate, values taken for the strength at different times are plotted for tantalum. In all cases, the elastic behaviour is represented by the line from the origin to the HEL and is of slope given by Eq. 3. The HEL is measured from the height of the elastic precursor at 2 mm and that for BCC tantalum lies around that for Ti64 but at almost three times the corresponding value for the FCC Ni_3Al. An interesting feature of the response is that the rate of hardening is similar for all three materials over this stress range.

The unloaded and recovered defect substructures are presented in Fig. 12. The samples were loaded and recovered as described above and were then prepared for further mechanical testing or for transmission electron microscopy (TEM). They show clear differences highlighting their microstructure's response to the shock loading process. In all cases the shock level was ca. 10 GPa and the pulse was held for 1 μs.

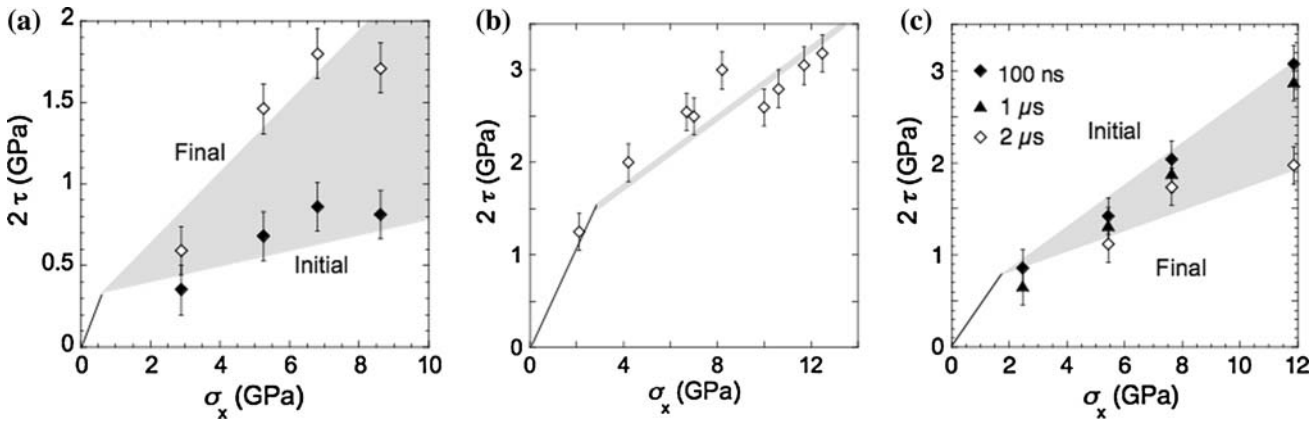

Fig. 11 Shear strength of **a** Ni_3Al, **b** Ti64 and **c** Ta as function of stress

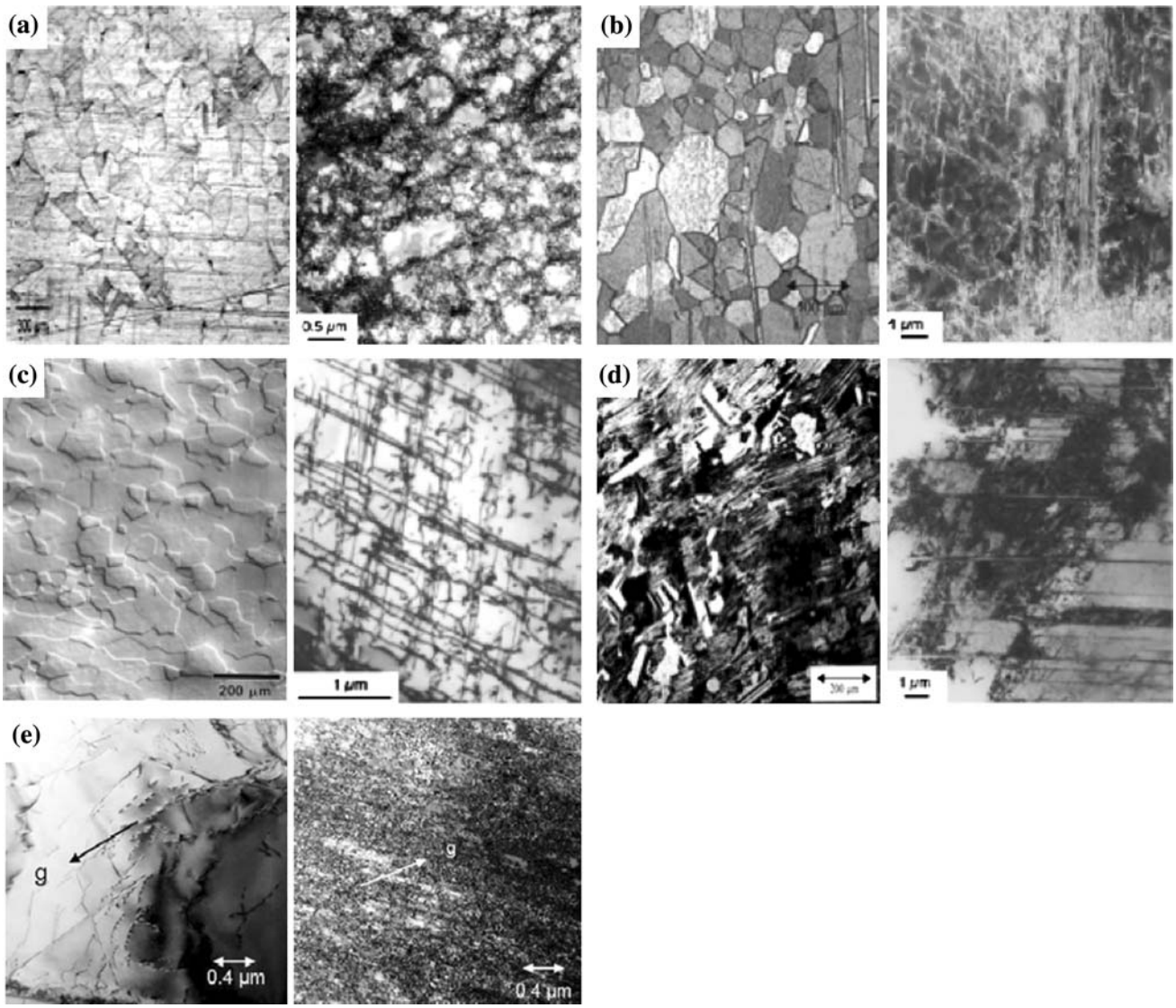

Fig. 12 Initial and recovered microstructures from the metals for nominally 1 μs pulses. **a** Nickel shocked to 10 GPa, **b** Ni_3Al shocked to 14 GPa, **c** Tantalum shocked to 7 GPa, **d** TiAl shocked to 10 GPa, **e** Ti64 shocked to 10 GPa

The TEM micrograph for the shock prestrained nickel is shown in Fig. 12a. The observed features show uniform dislocation cells in common with other polycrystalline FCC materials and with other workers [116]. It is interesting to note that those observed in the (100) and (111) single crystals were smaller (ca. 0.4–0.5 μm) than those seen in the polycrystalline nickel (0.6–0.8 μm) above, and that there was no readily apparent grain size effect (in the polycrystalline Ni-270 in Ref. [23]). Much more work has been done on materials subjected to lower strain rate loading and there the deformation substructure is similar to that observed in shock. It is clear that the material responds with similar micromechanical processes.

Figure 12b shows a substructure for shock prestrained Ni_3Al which shows a complex mixture of dislocation tangles, coarse planar slip bands comprising $\{111\}\langle 110\rangle$ dislocations, a few deformation twins and planar stacking faults. Deformation twins were seen to occur in samples shock loaded at a stress greater than 23.5 GPa where trace analysis showed the twinning plane to be of {111} type. Stacking faults have previously been found in cold-rolled Ni_3Al of the type $\{111\}1/3\langle 112\rangle$, which are superlattice stacking faults but their exact nature has not been quantified [139]. The coarse planar slip seen in the shocked Ni_3Al is much coarser than that observed in this material when deformed at lower strain rate [60].

Figure 12c shows micrographs of the annealed and the recovered and shock prestrained tantalum. The deformed material shows sets of long straight screw dislocations interspersed with dislocation tangles, small dislocation

cusps on the long straight screw dislocations and small dislocation loops and dislocation debris. The jogs and cusps in the screw dislocations formed by drag on the jogged screw dislocations under the high shear stresses imposed during shock loading, may account for the much lower mobility of screw as compared to edge segment dislocations. This restriction on screw dislocation mobility is thought to account for the persistence of long straight screw segments as well as the small dislocation loops and debris observed in shock-loaded tantalum [55].

Figure 12d shows the grain structure before loading and the substructure after in-shock prestrained Ti–48Al–2Nb–2Cr. Features observed were deformation twins and planar slip and were similar to that observed following high-strain-rate deformation in Ti–48–2–2 [66]. In that work, deformation twins were seen in the γ grains where the twins were often seen crossing planar laths of α_2 causing an offset in the α_2 laths. Deformation in the γ grains was also seen to consist of $\frac{1}{2}\langle 110\rangle$ dislocations [68].

Figure 12e shows micrograph from a Ti64 target recovered from a 10 GPa impact load. This result was part of an experimental program where a range of loading was applied with both a shock pulse and also with one with a slower rising edge to the same peak stress amplitude. The following observations were made [140]. Firstly the residual dislocation density increases with applied stress amplitude (and square pulse specimens contain a higher dislocation density than the step pulsed specimens). The deformation consists of planar slip in the square pulsed specimens. There were no twins when targets were loaded to 5 GPa but in the 10 GPa pulsed samples about 3% of the grains twinned. As with the previous work of Gray and Morris [76], no evidence of the α–ω phase transformation was detected.

In summary, the five metals discussed in this review show the following characteristic deformation features. The FCC nickel shows developed cells whereas Ni_3Al has responded with tangles and stacking faults. In BCC tantalum on the other hand, dislocations show long screws whereas in the intermetallic, TiAl, the structure shows long straight screw dislocations but also in this case some twinning. Ti64 shows similar microstructural features to the TiAl with planar arrays of dislocations and some twinning.

In order to understand the effect of shock prestraining on the post-shock-prestraining mechanical response of the materials discussed, both the annealed and shock-recovered samples were mechanically tested at a strain rate of 0.001 s^{-1}. The work on Ti64 is underway at present but the greatest differences are to found between the BCC and FCC metals. Figure 13 shows the stress–strain behaviour recorded for the tests conducted. If comparison of the effects of loading is to be useful, some account of the residual strain due to the shock loading and unloading strain path processes must be included to offset the reload curve relative to each materials unshocked behaviour. An estimate of this effective shock strain path may be recovered from the total shear strain undergone during shockwave loading,

$$\varepsilon_{\text{res}} = \frac{\sqrt{2}}{3}\left[(\varepsilon_x - \varepsilon_y)^2 + (\varepsilon_x - \varepsilon_z)^2 + (\varepsilon_y - \varepsilon_z)^2\right]^{\frac{1}{2}}. \quad (9)$$

Now in the case of shock loading the strain is one-dimensional and $\varepsilon_x = \varepsilon_y = 0$, leaving only ε_z. This simplified the equation for the strain in the shock state and recovers ε_{res} for the shock. Clearly before retest the material has also been released and assuming the two processes give the same strain gives a total effective strain

$$\varepsilon_{\text{res}} = \frac{4}{3}\ln\left(\frac{V}{V_0}\right), \quad (10)$$

where V and V_0 are the compressed and the original volumes of the specimen which can be recovered from the shock parameters through the conservation relations (Eq. 7) [113].

In all cases, the reload curves for the shocked metals have a higher yield stress than the annealed materials but

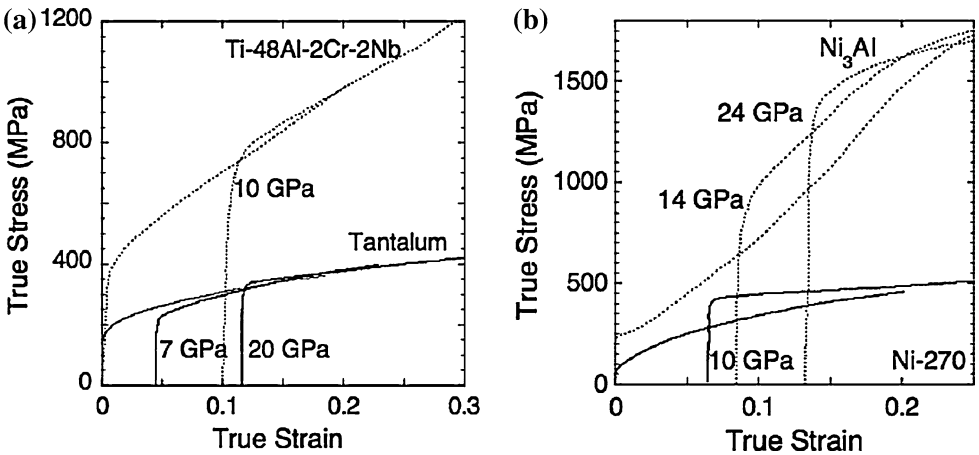

Fig. 13 Reload stress–strain behaviour at 0.001 s^{-1} for annealed and pre-shocked material. **a** TiAl and Ta showing no hardening behaviour, **b** Ni and Ni_3Al showing hardening on reload from the shocked state

when the curves are displaced by the residual effective strain different classes of behaviour are apparent. The figure is divided into two: (a) TiAl and Ta where the reload curves lie on one another, and (b) Ni and Ni_3Al where the reload curves all lie above the corresponding annealed ones at an equivalent strain level. Reloading samples previously shock prestrained thus illustrates shock strengthening for the FCC metals Ni and Ni_3Al, whilst showing no effect for BCC Ta and TiAl. It should be noted that the strain hardening appears to decline in the case of pure nickel while the Ni_3Al continues to strain harden with increasing plastic deformation following reloading even after shock prestraining.

This difference in effective shock hardening has been related to the fact that BCC metals have fewer operating slip systems than FCC crystals, since both these materials possess high Peierls stress and thus have greater resistances to defect motion through the lattice under shock loading conditions.

Figure 14 shows the strength measured at 1 μs after loading commenced in each material as a function of the longitudinal stress achieved at its peak. Previous discussion and strength histories such as those shown in Fig. 10 show that 1 μs represents a time by which stress equilibration appears to be complete in these materials. Some of the metals considered are seen to strengthen and some to soften behind the shock but here comparison is made at a time where the strength considered is stable. Over the stress range presented above, the metals all show a small elastic rise and then strength increases monotonically with impact

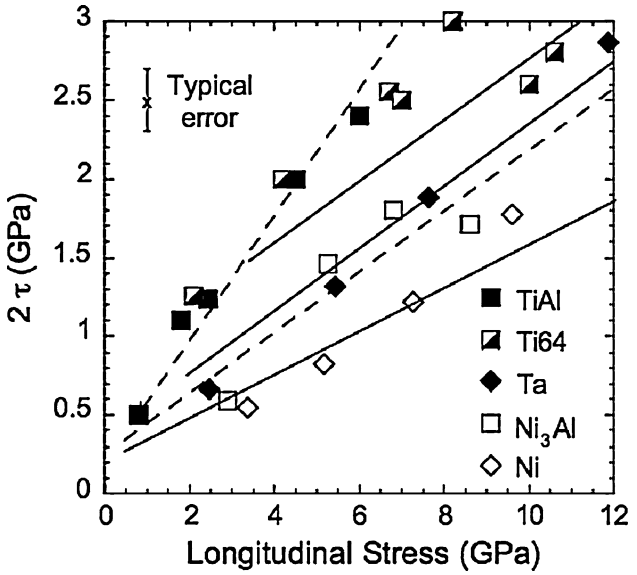

Fig. 14 Strength achieved at 1 μs into the pulse by each material as a function of the longitudinal stress at its peak. The solid lines show the hardening behaviour for Ta, Ni, and Ti64. The dotted curves show the hardening for the intermetallic materials

stress in the plastic region for each. However for pressures higher than those considered here other mechanisms such as shock heating dominate which causes strength to decrease towards the point at which there is shock melting in each material. Interestingly, a similar behaviour has been shown to occur in a range of materials up to ca. 40 GPa in a diamond cell where the loading was isothermal so that shock heating was not present and only single crystals were sampled [134]. In this case however, the material was still stronger than loading under shock. This comparison and discussion demonstrates the importance of strength considerations in even high amplitude dynamic loading where previously it has been regarded sufficient to assume the loading was hydrodynamic.

The examples chosen above show the effect of crystal structure upon characteristic behaviours with some showing pronounced shock strengthening (like the FCC metals Cu and Ni) while others do not (such as HCP Ti64). A further class of metals softens (BCC Ta discussed here, but also Nb and W). A key determinant of the behaviour of each class of materials is the Peierls stress to be overcome for slip to occur with high values (such as found in Ta and TiAl) reducing dislocation mobility dramatically during high-strain rate or low temperature deformation. In low Peierls stress materials such as Cu and Ni dislocations nucleate more easily, travel and interact more quickly and form dislocation tangles and/or cells resulting in strengthening of the material as a result of the shock loading pulse. A secondary important mechanism to accommodate the applied strain during shock loading is deformation twinning which occurs more readily in low symmetry materials than defect interaction mechanisms although it may not result in any greater degree of strain hardening. The key observation however is that shock experiments give a means of not only observing micromechanical effects upon continuum behaviour but also of probing the kinetics of the operating mechanisms and filtering the regime of dominance in controlling plastic accommodation processes of each by changing the peak stress and time interval of the impulse applied to separately examine stress and kinetic effects.

Conclusions

This article has reviewed research that has led to the current state of understanding of the response of metals to a shock loading compressive pulse. It has not extended to include phase transformation, release or spall behaviour but clearly the physical response in the compression phase is mirrored in tension since it also derives from a defect distribution in this mode, although in this case under release and thereafter tension. The magnitudes of the pulses

considered that have been discussed here lie in the range where thermal activation controls the dislocation nucleation and transport.

In summary, the sequence of events occurring after an impulsive load is applied to a metal appears to be as follows. (i) $t = 0$; impact takes the material to an elastic state indicative of a perfect crystal, (ii) $t = 0$(100 ps); defect activation which leads to relaxation of the elastic state to a plastic one, (iii) $t = 0$(100 ps); phase transformation (if relevant), iv) $t = 0$(1 ns) twinning, (v) $t = 0$(10 ns) slip, (vi) $t = 0$(100 ns) dislocation interaction and locking (strain hardening) or recovery, (vii) $t = 0$(1 μs) new defect source activation as defects are pinned, (viii) $t = 0$(1 μs) recrystallization, (ix) $t = 0$(10 μs) localization of plastic flow; adiabatic shear bands (N.T. Park, 2008, Private communication) [141].

There are a hierarchy of defect generation and storage processes and attendant microstructural features that determine the response to a step load. These affect critical parameters that influence observed response at the continuum; the activation threshold for plastic flow to occur, the kinetics with which it can proceed and the manner and effectiveness by which a material stores or accumulates that defect population. The temperature dependence of these is a further influence on each of these processes and events. The discussion above has introduced a series of experimental techniques used to probe shock loading in materials and shown their results upon a representative series of model materials. A key determinant of the mechanism and its kinetics is the atomic packing of the metal, since this determines the preferred processes and the planes and directions down which deformation occurs. The cubic metals have twelve possible slip systems whereas the HCP lattice has only two. Further, the Peierls stress required to slip planes of atoms further restricts the deformation that an impulse may accommodate by dislocation motion. The critical initial condition that controls all of these processes is the initial defect population within the material and that fixes both the positions from which slip can begin and also the travel that a dislocation may have before it locks with others or intersects a boundary. If slip is restricted, then a proportion of the strain may be accommodated via twinning.

All of these plastic processes are reflected in the observed form of the response in terms of both the evolved substructure as well as the post-mortem mechanical behaviour. The materials with the lowest density of mobile dislocations are BCC metals and they exhibit the slowest rise time for their plastic waves compared to the rapid rise in pure FCC materials where the number of accessible systems is high since the Peierls stress is low. Further, global strength measurement shows that FCC materials can achieve the plastic state quickly after the step loading on the impact face whereas BCC materials appear to only relax to the plastic state after hundreds of nanoseconds. This is reflected in the phenomenon known as precursor decay which describes the relaxation of the HEL of the metal with distance into the target (time for dislocation processes to act) which occurs over long distances for BCC metals [142]. Further it has been shown that the density and interactions of dislocations in these FCC materials result in them strengthening over a 1 μs impulse resulting in a higher reload strength. HCP metals have a lower Peierls stress than the BCC materials but their deformation is restricted by the symmetry of their structure which means that there are fewer slip systems available to them. On the one hand, this favours accommodation of the compressive strain by twinning as well as slip and on the other leads to an importance of texture in the response of HCP metals [140].

This review has aimed to show that the understanding of impulsive loading on materials requires linkage of the continuum scale measurements in testing to the microstructural observations from recovery experiments. It is the continuum response that drives the application of a material to its operational environment but to understand materials' deformation and to construct a physical description of its response, requires information from the meso-, micro- and atomic scale processes that occur. The available data indicate that the processes occurring at the atomic scale, such as phase transformation are well described by methods to derive atomic potentials so that thresholds can be accurately modelled with advanced quantum mechanical techniques even when the electron states are complex [143, 144]. Processes leading to plastic deformation are however dependent upon defect populations, their activation and subsequent interaction and these processes occur over times that map to length scales at the micro- and mesoscales. The evidence presented shows an evolving microstructure that must be described by analytical models that also evolve if the response is to be captured at the continuum. Existing descriptions, derived using continuum tests for quasi-static loading, will function well for the regime to which they were fit. However, these models cannot describe transient loading and the next generation of constitutive models must account for the operating physics if they are to be useful for this class of problems.

Finally, the range of theatres available to an experimental community must be selected with a mind to the material length and kinetic time scales that they can access. There is only a limited amount of information appropriate to description of the material state at the continuum that may be accessed by lasers or DACs probing perfect crystal volume elements at the atomic scale. Thus in isolation these devices can only yield results pertinent to the

construction of equations of state for pure materials. Rather, it requires launchers (Z pinch, gun or HE loading) to access the micro- and mesoscale where the key physics resides that fixes the material strength and damage evolution at the continuum.

The inhomogeneity of nature results in materials that deform accessing key physics tied to their crystal structures and the inherent defects within their volumes. It is the appreciation of these statistical physical relationships and their effects upon metallic response that will drive the development of these materials for use under extreme conditions in the future.

Acknowledgements NKB acknowledges the efforts of students who have worked on these issues and the funding bodies within UK government who have supported this work including EPSRC, DSTL, AWE and QQ. Also the useful discussions with workers in the different experimental and modelling techniques are discussed. GTG acknowledges the support of Los Alamos National Laboratory that is operated by LANS, LLC, for the National Nuclear Security Administration of the US Department of Energy under contract DE-AC52-06NA25396 and the Joint DoD/DOE Munitions Technology Development Program.

Appendix: Materials data

See Tables 1, 2, 3, 4, 5, 6.

In all cases, the material properties of all materials in this investigation were determined using quartz transducers operating at 5 MHz, with a Panametrics PR5077 pulse receiver. These are presented in Table 5.

Table 1 Pure nickel composition in weight%

Nickel grain size—ca 200 μm							
C	Si	Mn	P	S	Al	Co	Cr
<0.0005	0.002	<0.001	<0.001	<0.001	<0.001	0.021	<0.001
Cu	Fe	Mg	Ni	Ti	Pb ppm	Zn ppm	O
0.021	0.008	<0.001	Bal.	<0.001	<5	<10	0.0058

Table 2 Chemical composition of tantalum in weight%

C	O	N	H	W	Nb	Ti	Fe
10 ppm	<50 ppm	<10 ppm	<5 ppm	<25 ppm	<25 ppm	<5 ppm	<5 ppm

Table 3 Composition of Ni_3Al (at.%)

Al	B	O	C	N	P	S
24.1	0.095	0.03	0.02	0.007	0.005	0.002

Table 4 Composition (in at.%) of the TiAl alloys used in this study

	Ti	Al	Cr	Nb	B	Fe	Si	C	O	N
TiAl1	Bal.	46.5	2	1.9	–	0.077	0.069	0.019	0.192	0.025
TiAl2	Bal.	48	2	2	1	–	–	–	–	–

Table 5 Materials' properties

	c_L (mm μs^{-1})	c_S (mm μs^{-1})	c_B (mm μs^{-1})	ρ_0 (g cm^{-3})	ν
Nickel	5.83 ± 0.03	3.03 ± 0.03	4.66 ± 0.03	8.90 ± 0.01	0.315
Tantalum	4.13 ± 0.03	2.04 ± 0.03	3.39 ± 0.03	16.58 ± 0.01	0.339
Ni_3Al	6.23 ± 0.03	3.17 ± 0.03	5.04 ± 0.03	7.40 ± 0.01	0.325
TiAl1	7.36 ± 0.03	4.12 ± 0.03	5.62 ± 0.03	3.99 ± 0.01	0.260
TiAl2	7.29 ± 0.03	4.25 ± 0.03	5.39 ± 0.03	3.95 ± 0.01	0.250
Ti–6Al–4V	6.13 ± 0.03	3.13 ± 0.03	5.12 ± 0.03	4.40 ± 0.01	0.324

Table 6 Shock properties for the five materials taken from Marsh [131], Gray and Morris [76], Millett et al. [86, 87]

	ρ (kg m^{-3})	c_0 (mm μs^{-1})	Z	S
Ta	16.6	3.4	68.72	1.20
Ni	8.87	4.6	51.36	1.44
Ni_3Al	7.40	4.5	46.10	2.31
Ti–6Al–4V	4.40	5.1	26.97	1.08
TiAl	3.99	4.4	29.37	2.92

References

1. Meyers MA, Aimone CT (1982) J Met 35:A55
2. Hopkinson B (1905) Proc R Soc Lond 74:498
3. Hopkinson B (1914) Proc R Soc Lond A 89:411
4. Hopkinson J (1872) Proc Manch Lit Philos Soc 11:40
5. Armstrong RW, Walley SM (2008) Int Mater Rev 53(3):105
6. Field JE, Walley SM, Bourne NK, Huntley JM (1994) J Phys IV France Colloq C8 (DYMAT 94) 4:3
7. Edwards M (2006) Mater Sci Technol 22:453
8. Tresca H (1878) Proc Inst Mech Eng 30:301
9. Barré de Saint Venant AJC (1883) Théorie de l'Élasticité des Corps Solides de Clebsch. Dunod, Paris, p 480a–d (final note to para 60)
10. Orowan E (1946) Trans Inst Eng Shipbuild Scotl 89:165
11. Taylor GI (1946) J Inst Civil Eng 26:486
12. Whiffin AC (1948) Proc R Soc Lond A 194:300
13. Kolsky H (1949) Proc Phys Soc Lond B 62B:676
14. Gray GT III (2000) In: ASM handbook, mechanical testing and evaluation. ASM International, Materials Park, OH, p 462
15. Pisarenko GS, Krasowsky AY, Vainshtock VA, Kramerenko IV, Krasiko VN (1987) Eng Fract Mech 28:539
16. Meyers MA, Subhash G, Kad BK, Prasad L (1994) Mech Mater Sci Technol 17:175
17. Steinberg DJ, Lund CM (1989) J Appl Phys 65(4):1528
18. Hoge KG, Mukherjee AK (1977) J Mater Sci 12:1666. doi: 10.1007/BF00542818
19. Zerilli FJ, Armstrong RW (1987) J Appl Phys 61(5):1896
20. Zerilli FJ, Armstrong RW (1990) J Appl Phys 68(4):580
21. Zerilli FJ, Armstrong RW (1992) Acta Metall Mater 40:1803
22. Follansbee PS (1986) In: Murr LE, Staudhammer K, Meyers MA (eds) Metallurgical applications of shock-wave and high-strain-rate phenomena. Marcel Dekker, p 451
23. Follansbee PS, Gray GT III (1991) Int J Plast 7:651
24. Follansbee PS, Kocks UF (1988) Acta Metall Mater 36(1):81
25. Regazzoni G, Kocks UF, Follansbee PS (1987) Acta Metall Mater 35(12):2865
26. Preston DL, Tonks DL, Wallace DC (2003) J Appl Phys 93:211
27. Rosenfield AR, Votava E, Hahn GT (1968) In: Ductility. American Society of Metals, Metals Park, OH, p 63
28. Wright TW (2002) The physics and mathematics of adiabatic shear bands. Cambridge University Press, Cambridge
29. Asay JR, Hall CA, Konrad CH, Trott WM, Chandler GA, Fleming KJ, Holland KG, Chhabildas LC, Mehlhorn TA, Vesey R, Trucano TG, Hauer A, Cauble R, Foord M (1999) Int J Impact Eng 23:27
30. Armstrong RW, Arnold W, Zerilli FJ (2007) Metall Mater Trans A 38A(11):2605
31. Esquivel EV, Murr LE (2006) Mater Sci Technol 22(4):438
32. Schneider MS, Kad B, Kalantar DH, Remington BA, Kenik E, Jarmakani H, Meyers MA (2005) Int J Impact Eng 32:473
33. Bacon DJ, Vitek V (2002) Metall Mater Trans A 33(3):721
34. Feng C, Murr LE, Niou CS (1996) Metall Mater Trans A 27(7):1773
35. Hines JA, Vecchio KS (1997) Acta Mater 45:635
36. Arnold W, Held M, Stilp AJ (1990) In: Schmidt SC, Johnson JN, Davidson LW (eds) Shock compression of condensed matter—1989. Elsevier, Amsterdam, p 421
37. Johnson JN (1981) J Appl Phys 52:2812
38. Johnson JN (1982) In: Nellis WJ, Seaman L, Graham RA (eds) Shock waves in condensed matter—1981. American Institute of Physics, New York, p 438
39. Davison LW, Graham RA (1979) Phys Rep 55:255
40. Rose MF, Berger TL, Inman MC (1967) Trans Metall Soc AIME 239:1998
41. Kressel H, Brown N (1967) J Appl Phys 38:1618
42. Grace FI (1969) J Appl Phys 40:2649
43. Murr LE, Kuhlmann-Wilsdorf D (1978) Acta Metall 26:847
44. Wright RN, Mikkola DE (1982) Mater Sci Eng 53:273
45. Greulich F, Murr LE (1979) Mater Sci Eng 39:81
46. Gray GT III (1992) In: Meyers MA, Murr LE, Standhammer KP (eds) Shock-wave and high strain rate phenomena in materials. Marcel Deker, New York, p 899
47. Meyers MA, Kestenbach HJ, Soares CAO (1980) Mater Sci Eng 45:143
48. Murr LE, Huang J-Y (1975) Mater Sci Eng 19:115
49. Walsh JM, Rice MH, McQueen RG, Yarger FL (1957) Phys Rev 108:196
50. Rohde RW, Towne TL (1971) J Appl Phys 42:878
51. Furnish MD, Chhabildas LC, Steinberg DJ (1994) Dynamical behaviour of tantalum. American Institute of Physics, New York, p 1099
52. Mitchell AC, Nellis WJ (1981) J Appl Phys 52:3363
53. Furnish MD, Lassila DH, Chhabildas LC, Steinberg DJ (1996) In: Schmidt SC, Tao WC (eds) Shock compression of condensed matter—1995. AIP Press, Woodbury, NY, p 527
54. Fiske PS, Holmes N, Lassila D (1999) In: Khan AS (ed) Plasticity 99: constitutive and damage modelling of inelastic deformation and phase transformation, Neat Press, Fulton, MD, p 639
55. Gray GT III, Vecchio KS (1995) Metall Mater Trans A 26A:2555
56. Gray GT III (1990) In: Schmidt SC, Johnson JN, Davison LW (eds) Shock compression of condensed matter—1989. North-Holland, Amsterdam, p 407
57. Murr LE, Meyers MA, Niou C-S, Chen YJ, Pappu S, Kennedy C (1997) Acta Mater 45:157
58. Hsiung LM, Lassila DH (1998) Scr Mater 38:1371
59. Kear BH, Wilsdorf HGF (1962) Trans Metall Soc AIME 224:382
60. Sizek HW, Gray GT (1993) Acta Metall Mater 41:1855
61. Gray GT III (1993) In: Schmidt SC, Samara GA, Ross M (eds) High pressure science and technology. AIP Press, Colorado Springs, CO, p 1161
62. Albert DE, Gray GT (1994) Philos Mag A 70:145
63. Kasantseva NV, Greenberg BA, Popov AA, Shorokhov EV (2003) J Phys IV 110:923
64. Geng HY, Chen NX, Sluiter MHF (2005) Phys Rev B 71:012105
65. Kim Y-W (1991) Mater Res Symp Proc 213:777
66. Maloy SA, Gray GT (1996) Acta Mater 44:1741
67. Gardiner P, Miguelez H, Cortes R, LePetitcorps Y, Dodd B, Navarro C (1997) J Phys IV Colloq C3:593
68. Gray GT III (1994) J Phys IV Colloq C8:373
69. Jones IP, Hutchinson WB (1981) Acta Metall 29:951
70. Peters JO, Ritchie RO (2000) Eng Fract Mech 67:193
71. Thompson SR, Ruschau JJ, Nicholas T (2001) Int J Fatigue 23:5405

72. Ruschau JJ, Nicholas T, Thompson SR (2001) Int J Impact Eng 25:233
73. Kad BK, Schoenfeld SE, Burkins MS (2002) Metall Mater Trans A 33A:937
74. Kad BK, Schoenfeld SE, Burkins MS (2002) Mater Sci Eng A322:241
75. Schoenfeld SE, Kad BK (2002) Int J Plast 18:461
76. Gray GT III, Morris CE (1988) In: Sixth world conference on titanium, France, p 269
77. Rosenberg Z, Mebar Y, Yaziv D (1981) J Phys D Appl Phys 14:261
78. Dandekar DP, Spletzer SV (2000) In: Furnish MD, Chhabildas LC, Hixson RS (eds) Shock compression of condensed matter 1999. American Institute of Physics, Melville, NY, p 427
79. Razorenov SV, Kanel GI, Utkin AV, Bogach AA, Burkins M, Gooch WA (2000) In: Furnish MD, Chhabildas LC, Hixson RS (eds) Shock compression of condensed matter—1999. AIP Press, Melville, NY, p 415
80. Church PD, Andrews T, Bourne NK, Millett JCF (2001) In: Furnish MD, Thadhani NN, Horie Y (eds) Shock compression of condensed matter 2001. American Institute of Physics, Melville, NY, p 511
81. Tyler C, Millett JCF, Bourne NK (2006) In: Furnish MD (ed) Shock compression of condensed matter—2005. AIP Press, Melville, NY, p 674
82. Greeff CW, Trinkle DR, Albers RC (2001) J Appl Phys 90:2221
83. Millett JCF, Whiteman G, Bourne NK (2008) J Appl Phys 104(7):073531
84. Millett JCF, Meziere YJE, Bourne NK (2007) J Mater Sci 42:5941. doi:10.1007/s10853-007-1716-5
85. Gray GT III, Bourne NK, Millett JCF (2003) J Appl Phys 94:6430
86. Millett JCF, Meziere YJE, Gray GT, Cerreta EK, Bourne NK (2006) J Appl Phys 100:063506
87. Millett JCF, Bourne NK, Gray GT III, Jones IP (2002) Acta Mater 50:4801
88. Kalantar DH, Belak JF, Collins GW, Colvin JD, Davies HM, Eggert JH, Germann TC, Hawreliak J, Holian BL, Kadau K, Lomdahl PS, Lorenzana HE, Meyers MA, Rosolankova K, Schneider MS, Sheppard J, Stolken JS, Wark JS (2005) Phys Rev Lett 95(7):075502
89. Bridgman PW (1931) The physics of high pressure. Bell, London
90. McMillan PF (2005) Nat Mater 4(10):715
91. Rosenberg Z, Bourne NK, Millett JCF (2007) Meas Sci Technol 18:1843
92. Barker LM, Hollenbach RE (1972) J Appl Phys 43:4669
93. Bourne NK (1999) In: Cameron IG (ed) New models and numerical codes for shock wave processes in condensed media. AWE Hunting Brae, Aldermaston, Berkshire, UK, p 237
94. Dandekar DP, Weisgerber WJ (1999) Int J Plast 15:1291
95. Clifton RJ, Klopp RW (1985) In: Metals handbook. American Society of Metals, Metals Park, OH, p 230
96. Asay JR, Chhabildas LC, Dandekar DP (1977) Bull Am Phys Soc 24:712
97. Lipkin J, Asay JR (1977) J Appl Phys 48:182
98. Chhabildas LC, Wise JL, Asay JR (1981) Bull Am Phys Soc 26:666
99. Huang H, Asay JR (2006) J Appl Phys 100:043514
100. Brar NS, Bless SJ (1992) High Press Res 10:773
101. Rosenberg Z, Partom Y, Yaziv D (1981) J Appl Phys 52:755
102. Chartagnac PF (1982) J Appl Phys 53:948
103. Gupta SC, Gupta YM (1985) J Appl Phys 57:2464
104. Millett JCF, Bourne NK, Rosenberg Z (1996) J Phys D 29:2466
105. Rosenberg Z, Partom YJ (1985) J Appl Phys 58:3072
106. Rosenberg Z, Yaziv D, Partom Y (1980) J Appl Phys 51:3702
107. Bourne NK, Gray GT III (2005) Proc R Soc Lond A 460:3297–3312
108. Bourne NK, Gray GT III (2005) Soft-recovery of shocked polymers and composites. J Phys D Appl Phys 38(19):3690–3694
109. Bourne NK, Green WH, Dandekar DP (2006) On the one-dimensional recovery and microstructural evaluation of shocked alumina. Proc R Soc Lond A 462(2074):3197–3212
110. Dieter GE (1961) In: Shewmon PG, Zackay VF (eds) Response of metals to high velocity deformation. Interscience, New York, p 409
111. Llorca F, Buy F, Farre J (2002) In: Furnish MD, Thadhani NN, Horie Y (eds) Shock compression of condensed matter—2001. American Institute of Physics, Melville, NY, p 638
112. Mahajan S (1970) Phys Status Solidi A 2:187
113. Meyers MA (1994) Dynamic behavior of materials. Wiley-Interscience, New York
114. Mogilevskii MA (1985) Combust Explos Shock Waves 21:639
115. Mogilevsky MA, Newman PE (1983) Phys Rep 97:357
116. Murr LE (1981) In: Meyers MA, Murr LE (eds) Shock waves and high strain rate phenomena in metals. Plenum, New York, p 753
117. Murr LE, Meyers MA (1983) In: Blazynski TZ (ed) Explosive welding, forming and compaction. Applied Science Publishers, London, p 83
118. Smith CS (1958) Trans Metall Soc AIME 214:574
119. Zukas EG (1966) Metals Eng Q 6(2):1
120. Clifton RJ, Raiser G, Ortiz M, Espinosa H (1990) In: Schmidt SC, Johnson JN, Davidson LW (eds) Shock compression of condensed matter—1989. Elsevier, Amsterdam, p 437
121. Hagelberg CR, Swift RP, Carney TC, Greening D, Hiltl M, Nellis WJ (2000) In: Furnish MD, Chhabildas LC, Hixson RS (eds) Shock compression of condensed matter—1999. American Institute of Physics, Melville, NY, p 1275
122. Nellis WJ, Gratz AJ (1993) Int J Impact Eng 14:531
123. Norwood FR, Graham RA, Sawaoka A (1986) In: Gupta YM (ed) Shock waves in condensed matter—1985. Plenum, New York, p 837
124. Rabie RL, Vorthman JE, Dienes JK (1984) In: Asay JR, Graham RA, Straub GK (eds) Shock waves in condensed matter—1983. North-Holland, Amsterdam, p 199
125. Tanaka K, Fujiwara S, Kusakabe M (1984) In: Asay JR, Graham RA, Straub GK (eds) Shock waves in condensed matter—1983. North-Holland, Amsterdam, p 203
126. Gray GT III (1993) In: Asay JR, Shahinpoor M (eds) High-pressure shock compression of solids. Springer-Verlag, New York, p 187
127. Gray GT III (2000) In: Kuhn H, Medlin D (eds) ASM handbook. Vol 8: mechanical testing and evaluation. ASM International, Materials Park, OH, p 530
128. Gray GT III, Follansbee PS, Frantz CE (1989) Mater Sci Eng A 111:9
129. Jones OE (1972) In: Davison L, Kennedy JE (eds) Behavior and utilization of explosives in engineering design. University of New Mexico, Albuquerque, NM, p 125
130. Stevens AL, Jones OE (1972) Trans ASME J Appl Mech 39:359
131. Marsh SP (1980) LASL shock hugoniot data. University of California Press, Los Angeles
132. Duvall GE, Graham RA (1977) Rev Mod Phys 49:523
133. Hsiung L (2000) Acta Mater 48(20):4865
134. Duffy TS (2007) In: Furnish MD et al (eds) Shock compression of condensed matter 2007. American Institute of Physics, Melville, NY, p 639
135. Zaretsky EB, Kanel GI, Razorenov SV, Baumung K (2005) Int J Impact Eng 31:41
136. Kanel GI, Razorenov SV, Baumung K, Singer J (2001) J Appl Phys 90:136

137. Millett JCF, Bourne NK, Rosenberg Z, Field JE (1999) J Appl Phys 86(12):6707
138. Millett JCF, Gray GT III, Bourne NK (2007) J Appl Phys 101:033520
139. Kear BH, Giamei AF, Oblak JM (1970) Scr Metall 4:567
140. Ming C, Millett JCF, Bourne NK, Jones IP (2008) J Appl Phys (in press)
141. Shehadeh MA, Bringa EM, Zbib HM, McNaney JM, Remington BA (2006) Appl Phys Lett 89(17):171918
142. Taylor JW, Rice MH (1963) J Appl Phys 34:364
143. Taioli S, Cazorla C, Gillan MJ, Alfe D (2007) Phys Rev B 75(21):214103
144. Cazorla C, Alfe D, Gillan MJ (2008) Phys Rev B 77(22):224103